Marine Structures 79 (2021) 103059

Contents lists available at ScienceDirect

Marine Structures

journal homepage: www.elsevier.com/locate/marstruc

Experimental field study of floater motion effects on a main bearing in a full-scale spar floating wind turbine

Jone Torsvik *, Amir R. Nejad, Eilif Pedersen

Norwegian University of Science and Technology (NTNU), Department of Marine Technology, Otto Nielsens vei 10, 7491 Trondheim, Norway

ARTICLE INFO

Keywords:
Floating wind turbine
Main bearing
Strain measurement
Bearing deflection
Decoupled analysis
Nonlinear behaviour

ABSTRACT

In this paper we present a full-scale experimental field study of the effects of floater motion on a main bearing in a 6 MW turbine on a spar-type floating substructure. Floating wind turbines are necessary to access the full offshore wind power potential, but the characteristics of their operation leave a gap with respect to the rapidly developing empirical knowledge on operation of bottom-fixed turbines. Larger wind turbines are one of the most important contributions to reducing cost of energy, but challenge established drivetrain layouts, component size envelopes and analysis methods. We have used fibre optic strain sensor arrays to measure circumferential strain in the stationary ring in a main bearing. Strain data have been analysed in the time domain and the frequency domain and compared with data on environmental loads, floating turbine motion and turbine operation. The results show that the contribution to fluctuating strain from in-plane bending strain is two orders of magnitude larger than that from membrane strain. The fluctuating in-plane bending strain is the result of cyclic differences between blade bending moments, both in and out of the rotor plane, and is driven by wind loads and turbine rotation. The fluctuating membrane strain appears to be the result of both axial load from thrust, because of the bearing and roller geometry, and radial loads on the rotating bearing ring from total out-of-plane bending moments in the three blades. The membrane strain shows a contribution from slow-varying wind forces and floating turbine pitch motion. However, as the total fluctuating strain is dominated by the intrinsic effects of blade bending moments in these turbines, the relative effect of floater motion is very small. Mostly relevant for the intrinsic membrane strain, sum and difference frequencies appear in the measured responses as the result of nonlinear system behaviour. This is an important result with respect to turbine modelling and simulation, where global structural analyses and local drivetrain analyses are frequently decoupled.

1. Introduction

Larger turbines are a fundamental contribution to reducing cost of energy in offshore wind power. Extracting energy at higher altitudes increases the capacity factor. Fewer and larger turbines also reduce the number of installation operations and the number of access points for maintenance. Provided that cost per MW installed does not increase too progressively with turbine size, as discussed by Sieros et al. [1], that size in itself does not force a step change in foundation technology, and that service and installation vessels are available, project cost models will categorically favour larger turbines. The design challenge is, however, considerable. Main bearings are one area where technology is applied outside known envelopes as new turbines are developed. The need for compact

* Corresponding author.
E-mail addresses: Jone.Torsvik@ntnu.no (J. Torsvik), Amir.Nejad@ntnu.no (A.R. Nejad), Eilif.Pedersen@ntnu.no (E. Pedersen).

https://doi.org/10.1016/j.marstruc.2021.103059
Received 4 September 2020; Received in revised form 8 May 2021; Accepted 17 May 2021
Available online 28 July 2021

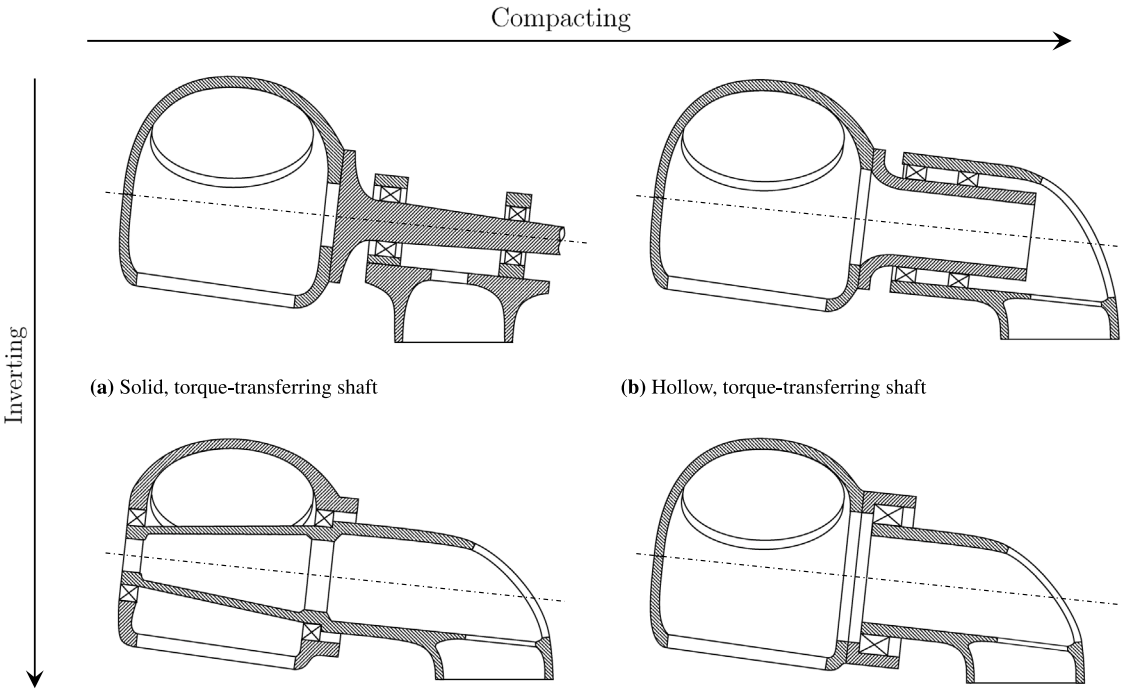

(a) Solid, torque-transferring shaft

(b) Hollow, torque-transferring shaft

(c) Inverted, multiple bearings on hollow, stationary shaft

(d) Inverted, single bearing on hollow, stationary shaft

Fig. 1. Different bearing layouts.

and lightweight designs prompts consideration of alternatives to solid main shafts supported by separate bearing blocks on a bed frame as illustrated in Fig. 1(a). One path is to leverage rolling-element bearing technology to let larger-diameter bearings with thinner sections support shell-like drivetrain structural elements as illustrated in Figs. 1(b–d). Thus, the main bearings themselves to some extent become parts of a continuous, hollow structure, not unlike like the blade bearings and some yaw bearings, yet with a very different mode of operation. In these designs, hub deformation is affecting the bearing, challenging the validity of a 5-Degree of Freedom (DOF) bearing model. The main bearings are in fact the first connection between the drivetrain and the supporting structure. They are often considered as a filter, blocking none-torque loads from being transmitted to other parts of the drivetrain.

The INNWIND project [2] was launched in 2012 in acknowledgement of the technological challenges of making 10 MW to 20 MW turbines. Stehouwer and van Zinderen [3] reports from a study of possible drivetrain layouts. The alternatives are all based on large-diameter tapered roller bearings with small sections and many rollers. Differences between the layouts are considered largely at the aeroelastic modelling level; besides giving component and nacelle masses for the different layouts, the report refers to aspects such as centre of gravity, static bending moments and blade-tower clearance. Furthermore, the report refers to the general use of Finite Element Analysis (FEA) for component level analyses, without disclosing any details of bearing calculations. With respect to feasibility, the report questions the availability of bearings for realizing the designs at the 20 MW upper bound, without referring to specific size limitations in manufacturing and transportation.

2020 saw the publication of National Renewable Energy Laboratory (NREL)'s and Technical University of Denmark (DTU)'s collaborative 15 MW reference model under International Energy Agency (IEA) Wind Task 37 [4]. To warrant a complete physical basis for analyses in the aeroelastic model domain, the reference model includes a description of a drivetrain using similar bearing technology as the INNWIND study, yet of slightly more conservative proportions. With reference to Smith [5], a double-row tapered roller bearing and a cylindrical roller bearing are used instead of two separate tapered roller bearings.

Introducing bearings at the edges of shell-like structures forces the consideration of bending stiffness and deflection in the bearing planes. Kabus and Pedersen [6] were future-oriented, hinting at potential challenges with large-diameter rolling-element bearings supported in flexible structures. Considering a hollow yet relatively thick-walled shaft supported in tapered roller bearings, they performed a structural optimization of the bearing supports using FEA. Kabus et al. [7] carried this work forward, deriving a multi-body time-simulation model that, unlike the simpler 6-DOF models, represents outer ring deflection, but is far more computationally efficient than the full Finite Element (FE) alternative. Dabrowski et al. [8,9] showed examples of the use of FEA for structural component optimization in targeting low mass for one of the INNWIND designs. Kock et al. [10] applied quasi-static FEA to the wind turbine main bearing supports in a drivetrain arrangement of fairly conventional layout and proportions, but still made the case in point that load distribution in main bearings should always be considered in multi-MW wind turbines and that the choice between elastic and rigid modelling of the bearing support significantly affects results.

Numerous studies on drivetrain dynamics followed in the wake of the reliability problems experienced in early gear-based drivetrains. Early examples include those by Peeters et al. [11] and Schlecht et al. [12,13], the latter pointing to structural flexibility as the reason why gears and bearings that work well in other industries fail in offshore wind and advocating the use of elastic bodies in modelling. Incremental contributions by Helsen et al. [14,15,16], Nejad et al. [17,18,19], Guo et al. [20,21] and others have since provided insight in the effects of drivetrain layout and flexibility and established flexible multi-body simulation as the state of the art in drivetrain modelling and analysis.

The natural frequencies of the drivetrain are higher than the natural frequencies of the global structure. Furthermore, traditional drivetrain configurations to some extent have discrete supports and simple load paths between the drivetrain and the global structure. Consequently, dynamic analyses of the drivetrain are often decoupled from dynamic analyses of the global structure. Coupled analyses are mainly seen in studies involving the electrical side of the drivetrain, where only the torsional dynamics of the mechanical system are considered, and a gearbox represents a significant compliance. Partly the result of how main bearings are treated in wind turbine-specific standards, detailed analyses of main bearings remain associated with the drivetrain domain. However, these are often limited to assess how main bearings affect the transfer of non-torque loads onto other parts of the drivetrain.

The above cited works on main bearings are all static or quasi-static, based on the decoupled approach and using loads derived from aeroelastic simulations as input. FEA can be employed in the drivetrain modelling domain to assess the bearing load distribution and the risk of skidding, but requires careful consideration of the structural complexity and how much of the surrounding structures to include, the boundary conditions, whether to use static or dynamic analyses, and which load cases to apply. Particularly important for hollow shaft designs is the consideration of hub deflection caused by blade bending moments.

Hart et al. [22] presented a comprehensive review of main bearing technology, addressing both hub loading spectra and different bearing layouts. However, the aspect of "hollowness" of the structure and the transmission of hub deflection onto the main bearing was not considered.

For floating offshore wind power development, the governing idea is that floating substructures accommodate the same standard turbines as used on bottom-fixed foundations. By economies of scale, this will help lower the cost of energy, particularly while floating offshore wind turbines are still in the introductory phase. According to this concept, floating operation should not have to be a design driver for wind turbines. Consequently, floating operation is currently being treated as a set of project-specific conditions for which the calculated ultimate loads and accumulated fatigue damage shall not exceed the standard turbine's type certification basis. While this can be achieved, the loads are different as the result of floater motion. For any given failure rate, a failed main bearing integrated into the structure such that the whole rotor-nacelle must be removed for repair also has more severe consequences in a floating wind turbine. Furthermore, floating operation does not yet have the benefit of experience building through deployments of similar turbines in large numbers. Although pioneering floating wind farms exist and more are under planning, these represent a variety of both turbine drivetrain designs and floating substructure designs.

The effects of floating operation on drivetrains have only to a limited extent been discussed in literature, and studies are mostly based on modelling and simulation. Using the NREL Gearbox Reliability Collaborative (GRC) 750 kW drivetrain model, Xing et al. [23] compared operation on an Offshore Code Comparison Collaboration (OC3) [24] spar-type floating substructure with operation on an bottom-fixed foundation, presenting the relative differences in drivetrain loads in terms of mean values, standard deviations and maximum values. A similar comparison was done between a three-point and a four-point version of the drivetrain for the Floating Wind Turbine (FWT) case. The study concluded that floating operation increases non-torque loads in the drivetrain, primarily in the low speed side. The most significant increase was seen in the locating main bearing axial load. As expected, the four-point suspension largely diminishes non-torque loads in the gearbox, leaving the main bearings loads as the main concern for floating operation. Nejad et al. [18] compared accumulated fatigue damage in the drivetrain mechanical parts from floating operation on an OC3 spar with bottom-fixed operation using the NREL 5 MW reference turbine [25] and the 5 MW reference drivetrain from Nejad et al. [17]. They also reported a significant increase in fatigue damage from axial load on the locating main bearing, noting that the bearing type is sensitive to axial load. Furthermore, Nejad et al. [19] studied the effect of floating operation on mechanical drivetrain components for different floating substructures—a Tension Leg Platform (TLP), a spar and two different semi-submersibles. It was shown that the locating main bearing sustained increased fatigue damage on all floating substructures compared to a fixed foundation as the results of bearing axial loads, the highest increase found on the spar substructure. Published experimental research on floating wind turbines is mainly based on scale models. Such studies are limited to considering drivetrain aspects on a global structural level. One example is Goupee et al. [26], who compared the performance of three different floating substructures and reported the corresponding turbine thrust forces.

The above contributions to understanding the effects of floating operation on drivetrain dynamics all indicate that further studies of the effects on main bearings are needed. Taking into account the main bearing development trends, such studies should also aim at assessing any effect on spatial deflection in the bearing and, considering the nonlinear characteristic of rolling element bearings, if local dynamics can be universally dealt with through decoupled analyses. To address these aspects, we want to experimentally study the effect of floating operation on non-torque loads and deflections in the main bearings in one of the world's first commercially operated wind farms based on spar substructures.

The wind power industry has a long history with experimental design verification. Load response measurements is included in type testing and certification processes, and warranted in, for example, the IEC System for Certification to Standards Relating to Equipment for Use in Renewable Energy Applications (IECRE System)'s operational document IECRE OD-501[27], which partly replaces the withdrawn standard IEC 61400-22[28]. Guidelines on measured quantities and sensor positions are given in IEC 61400-13[29]. These guidelines are primarily adapted to the verification of global structural analyses and aligned with the fidelity of industry-standard aeroelastic codes. Strain measurements are recommended for calculating bending and torsional moments in the

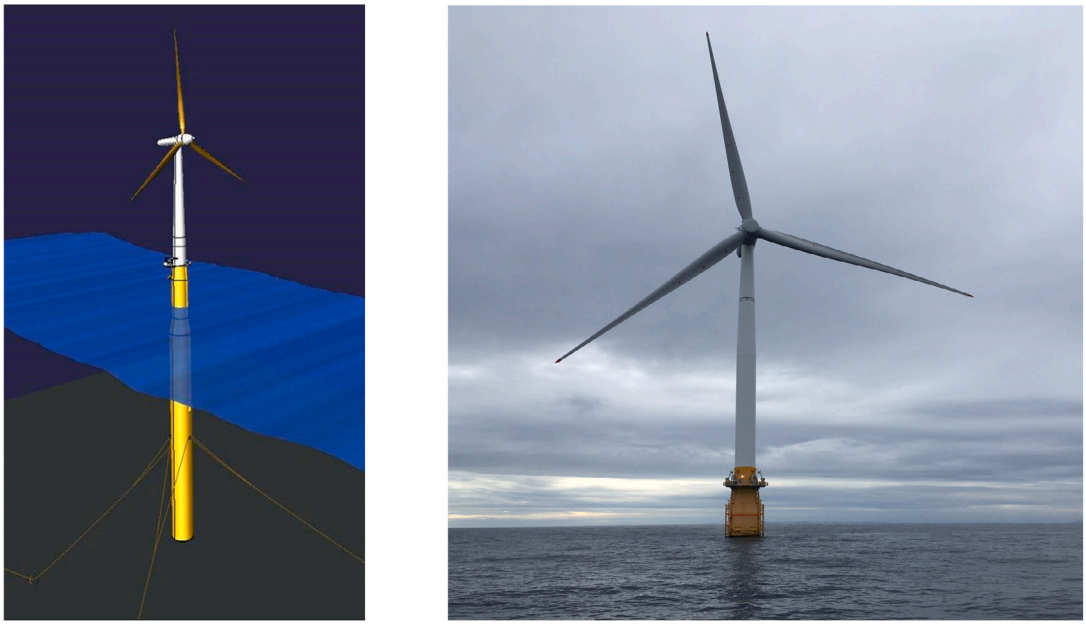

(a) (Illustration courtesy of Equinor) (b) (Photo by first author)

Fig. 2. Floating wind turbines on spar substructures.

turbine's shaft and tubular members. Deflections in the bearing planes are not specifically considered. International Electrotechnical Commission (IEC)'s drivetrain-specific standard IEC 61400-4 IEC [30] only applies to gearboxes. Det Norske Veritas Germanischer Lloyd (DNVGL)'s drivetrain-specific standard DNVGL-ST-0361[31], includes the hub in the drivetrain definition and acknowledges that emerging drivetrain solutions can take various forms, but provides limited detail and states that measurements shall be aimed at verifying model assumptions. Overall, it does appear that standardization work responds to a diverse solution space by focusing on procedural and functional aspects in order to maintain generality in requirements. The lack of visibility of design-specific considerations in standards and guidelines further motivates our search for knowledge on the effects of floating operation on main bearings for the design of future, above-10 MW turbines. This particularly regards the use of large-diameter, thin-section rolling element bearings.

Our approach is to equip two turbines with optical Fibre Bragg Grating (FBG) strain sensor arrays to measure circumferential strain in several positions in the same plane on the stationary bearing rings. This paper presents a first-tier analysis, with selected data presented and analysed in both the time and frequency domains, and the results summarized in a short discussion. Turbine-specific characterization is not an objective, and thus strain and deflection amplitudes are presented on consistent but undefined scales. Furthermore, the present analysis does not consider park effects or transient events.

2. Turbine and site description

The instrumented turbines are three-blade, upwind, horizontal-axis, pitch-controlled, rated 6 MW and placed on floating foundations of the spar type, as shown in Fig. 2(a,b). Identical equipment is installed in two out of a total of five turbines comprising a small farm. The farm spans approximately 4 square kilometres in water depths between 95 and 129 metres, and the distance to shore is approximately 24 kilometres.

The turbines' basic control and monitoring system provides wind speed, generator speed and rotor position. The wind speed anemometer is installed on top of the nacelle, in the wake of the rotor. The turbines are equipped with Motion Reference Units (MRUs) providing input to the floater motion controller. An instrumented buoy provides ten-minute statistical wave and current data.

3. Bearing measurements

To obtain data for the analysis, both the physical quantities to measure and the instrumentation to use had to be defined. Several circumstantial factors influenced the decision to measure circumferential strain using FBG sensor arrays.

First, the installation reflects an industry trend with larger and more advanced turbines having strain sensors permanently installed in the blades for monitoring and control. For permanent instrumentation, FBG strain sensors are favoured over electric

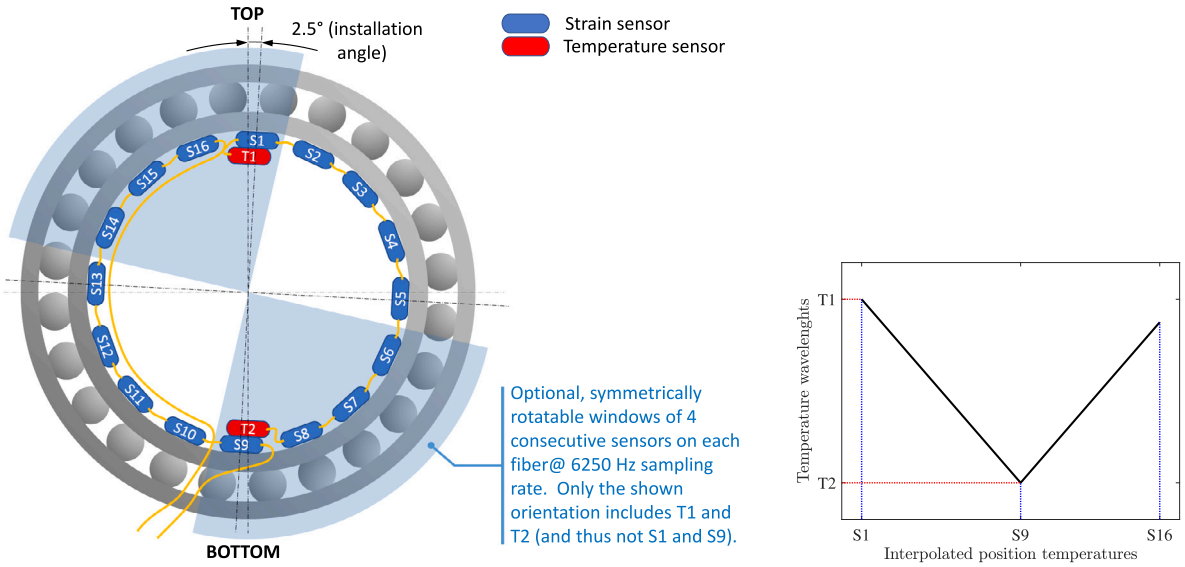

(a) Sensor positions viewed aft-fore.

(b) Interpolation between T1 and T2.

Fig. 3. Sensor positions and applied temperature profile for compensation.

strain gauges. The choice is further helped by the development of more compact and cost efficient FBG interrogators. A similarly durable setup and open-ended possibility for monitoring of the bearings were considered an improved return on investment.

Secondly, Hoffmann et al. [32] and others have investigated FBG-based strain measurements in rolling element bearings, reporting good sensitivity to roller passing and geometric disturbances. The present experiment presented an opportunity to use a similar setup on a low-speed, large-diameter, thin-section bearing, although without the need to exploit the advantage of FBG sensors that they can be embedded in small, dedicated grooves on a surface.

Lastly, a trial installation of the same type of sensors was performed on the main bearing in a similar but smaller onshore turbine, and promising initial results created interest in carrying over the concept for further testing.

3.1. Measured quantity

In analysing mechanical vibration, one has the choice between measuring acceleration, velocity and displacement, disregarded the different practical advantages and limitations with respect to sensor types and applications. Accelerometers provide a wide dynamic range, accentuate the high-frequency content and are generally preferred for frequency analysis. Strain is related to displacement and tends to be dominated by low-frequency content, where most of the energy usually lies. Deriving displacement from strain is, however, generally not straightforward, and requires a displacement–strain compatibility model to be established, as discussed in Section 3.3. In this experiment, the range of interest is from the quasi-static vibrations from floater motion and turbine global structural response to the first bending natural modes of the main bearing rings and supporting structures. Strain measurement was considered overall most beneficial as it captures both static and dynamic deflection, and ignores rigid-body motion. The main excitation is also low-frequency; 1P from non-symmetry or imbalance in the rotor, and 3P from wind shear, tower shadow and gravity. Excitation from internal bearing dynamics or from the generator might occur at higher frequencies.

The 16 strain sensors are equidistantly spaced and circumferentially aligned in a single plane on the back of the bearing stationary ring, providing ample spatial resolution. The available bandwidth of the system limits the sampling rate to 2500 Hz when using all sensors. A Nyquist frequency of 1250 Hz was considered marginal for capturing the bending natural modes; however, the measurement equipment offers a possibility for trading spatial resolution for temporal resolution. Up to a 6250 Hz sampling rate can be achieved for a subset of sensors, and identification of the first bending natural modes does not require that all the 16 sensors are used. The sensor positions and the possible sensor combinations for the 6250 Hz sampling rate are shown in Fig. 3(a).

3.2. Instrumentation

An FBG is a spatially-periodic variation in the refractive index over a small length of an optical fibre. Each of the variations reflects a small amount of light. As a result of the spatial periodicity these small reflections combine to a reflection of almost all the light in a very narrow-banded part of the spectrum, whereas the light in the remaining parts of the spectrum passes through. This property lends itself to strain measurement, as the spatial periodicity change with mechanical strain in the fibre, causing a shift in the wavelength of the reflected light. Multiple gratings can be interrogated on a single fibre provided that sufficient wavelength

separation is available, thus, the number is dependent on the grating sensitivity, the operating wavelength shift and the system bandwidth.

The conversion of wavelength to strain is based on assumed linear relationships and constant coefficients to represent material properties, except for the optical fibre refractive index, whose temperature dependence is compensated. Temperature measurement is included to also separate mechanical strain from total strain, and particularly relevant in the current application because of the local heating of the structure from bearing losses.

Temperature measurement is performed by leaving a number of gratings separate from the substrate, so that wavelength change only responds to temperature change. Based on an overall assessment of the application and the interrogation equipment, the 16 strain sensors were distributed onto two separate fibres, each having 8 strain sensors and one temperature sensor. As shown in Fig. 3(a), the temperature sensors T1 and T2 are in the top and bottom positions. The highest temperature gradient over the entire bearing is assumed to appear in the vertical direction, because of gravitational load. Linear interpolation between T1 and T2 is used for compensation of strain sensors S1–S16, as shown in Fig. 3(b).

The sensors were installed on the main bearing after the nacelle was assembled but before the hub and blades were attached. Baseline sensor readings without the effects of gravitational forces on the hub and the blades are therefore available.

Wavelength shifts caused by strain change and temperature change are calculated using the coefficients K_ε and K_T

$$\begin{aligned} \Delta\varepsilon &= K_\varepsilon \Delta\lambda_\varepsilon, \\ \Delta T &= K_T \Delta\lambda_T, \end{aligned} \tag{1}$$

where $\Delta\lambda_\varepsilon$ and $\Delta\lambda_T$ are the wavelength shifts of strain measuring FBGs and temperature-compensating FBGs. The total strain based on the measured wavelength shift $\Delta\lambda_{meas}$ is then taken as

$$\Delta\varepsilon_{tot} = K_\varepsilon \left(\Delta\lambda_{meas} - \frac{\Delta T}{K_T} \right), \tag{2}$$

The mechanical strain is then found as the total strain minus the strain caused by thermal expansion of the bearing material

$$\Delta\varepsilon_{mech} = \Delta\varepsilon_{tot} - \alpha_L \Delta T, \tag{3}$$

where α_L is the thermal expansion coefficient.

3.3. Displacement–strain compatibility

In numerical analysis, forcing functions must be defined correspondingly to the model's coordinates to excite responses for the different load cases considered. In mechanical engineering, design criteria frequently apply to strains, and forces and displacements are converted to stresses and strains through *strain–displacement relations*. Oliver et al. [33] states that strain always can be derived from displacement through differentiation, provided a reasonably uncomplicated displacement field. The opposite case is less straightforward; integrating strains to find a displacement field does not necessarily yield a solution. Certain conditions must be verifiable, such as continuity, by what is referred to as *compatibility conditions* or *compatibility equations*.

A pure design verification analysis could likely be based on the measured strains directly. Although this paper does not include numerical model verification, relating strain to displacement is of interest, also because displacement is more intuitive and analogously visualized.

The structure supporting the main bearing is essentially cylindrical, with heavier cross sections and increased stiffness in the bearing ring areas. As such, it is an appreciable case for establishing displacement–strain compatibility for the bearing stationary parts, given a set of simplifying assumptions.

First, Euler–Bernoulli theory is used for the bearing cross section as a closed circular beam, assuming that plane sections remains plane and normal to the neutral axis after deformation. Neglecting transverse shear deformation leaves only plane strain ε_θ to be considered. Seidel and Erdelyi [34] refer to a ratio of 1/10 or lower between ring thickness and ring neutral axis radius as rendering the Euler–Bernoulli assumption valid, which is not too far from the actual aspects in this application. It is also ignored that differential bending strain in a curved beam is not proportional to the distance from the neutral axis and that the neutral axis does not coincide with the centroid axis, as shown in Fig. 4.

Secondly, only motion in the bearing plane is considered, and expressed in the coupled coordinates u_R and u_θ, referred to as transverse and circumferential displacement. The restraining effect or Poisson effect in the longitudinal or shaft axis direction is ignored, as a simplification of general plate- and shell theory, yielding a simple ring model.

Per the simplifying assumptions, circumferential strain ε_θ consists of membrane strain ε_θ^0 and bending strain $\alpha_R K_\theta$,

$$\varepsilon_\theta = \varepsilon_\theta^0 + \alpha_R K_\theta, \tag{4}$$

where K_θ is the beam curvature change and α_R is the distance from the neutral axis at which bending strain is considered, in our case the beam inner surface. The membrane strain ε_θ^0 and the curvature change K_θ can be expressed in the circumferential and transverse coordinates u_θ and u_R as

$$\varepsilon_\theta^0 = \frac{1}{a} \left(\frac{\partial u_\theta}{\partial\theta} + u_R \right) \tag{5a}$$

$$K_\theta = \frac{1}{a} \frac{\partial\beta}{\partial\theta} = \frac{1}{a^2} \left(\frac{\partial u_\theta}{\partial\theta} - \frac{\partial^2 u_R}{\partial\theta^2} \right) \tag{5b}$$

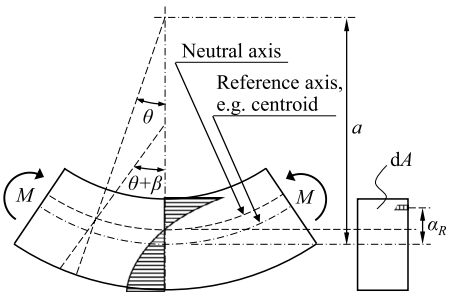

Fig. 4. Ring segment.

where a is the circular beam undisturbed neutral axis radius, and β is the beam transverse plane rotation angle from bending.

As is generally known from Euler–Bernoulli theory, longitudinal (extensional) vibrations in a beam typically have natural frequencies one order of magnitude higher than transverse (bending) vibrations. Consequently, circumferential forcing and circumferential inertial terms in a closed, circular beam are sometimes ignored. As shown by Soedel [35], introducing the relation $u_R = -\partial u_\theta/\partial\theta$ decouples the beam's two equations of motion, yielding a single equation in the transverse coordinate u_R. This is called the inextensional assumption, as the membrane strain vanishes.

Here, the membrane strain cannot be ignored because of the large static and quasi-static content. However, the contributions from extensional natural modes other than the $n = 0$ 'breathing mode' are assumed insignificant, and circumferential displacement is simply taken as equal in all positions, thus, $\frac{\partial u_\theta}{\partial\theta} = 0$. This means that membrane strain is separated from bending strain simply by taking the spatial average of the measured circumferential strain.

By combination of Eqs. (4) and (5b), Eqs. (5a) and (5b) can now be rewritten as

$$u_R = a\varepsilon_\theta^0. \tag{6a}$$

$$-\frac{\partial^2 u_R}{\partial\theta^2} = a^2\frac{\varepsilon_\theta}{\alpha_R}. \tag{6b}$$

Both the transverse deflection and the bending strain must be continuous and periodic, as each function and its derivatives must have the same value for $\theta = 0$ and $\theta = 2\pi$. The average bending strain must also be zero, as the membrane strain makes up any non-zero spatial average. Olver [36] shows that if a function is (piecewise) continuous and has mean zero on the interval $[-\pi, \pi]$, then its Fourier series expansion

$$\varepsilon_\theta(\theta) \sim \sum_{n=1}^{\infty}\left(A_n \sin n\theta + B_n \cos n\theta\right) \tag{7}$$

can be integrated term by term to produce the Fourier series

$$u_R = -\frac{a^2}{\alpha_R}\int_{-\pi}^{\pi}\int_{-\pi}^{\pi}\varepsilon_\theta(\theta)d\theta^2 \sim -\frac{a^2}{\alpha_R}m - \frac{a^2}{\alpha_R}\sum_{n=1}^{\infty}\left(-\frac{A_n}{n^2}\sin n\theta - \frac{B_n}{n^2}\cos n\theta\right), \tag{8}$$

where the constant term m is the mean of the integrated function. This means that the bending deflection and the bending strain are in spatially opposite phase, which is intuitive; positive strain or stretching corresponds to an inward transverse deflection or reduced radius. It also means that the displacement amplitude scales with both the strain amplitude and the inverse of the order number squared. Assuming that lower orders grossly dominate the deflection, strain is an acceptable approximation to displacement when plotting and comparing values on an undefined scale. Note that the first natural bending mode is at $n = 2$. As described in Soedel [35], there exist no $n = 0$ and $n = 1$ bending mode in a ring.

3.4. Uncertainty assessment

Any process by which some physical effect is quantified is affected by uncertainty, which can be classified as either epistemic or aleatory. Epistemic or *subjective* uncertainty stems from a lack of knowledge and can be reduced by increasing the number of samples and improving models and assumptions. Aleatory or *objective* uncertainty results from inherent randomness and is accepted as irreducible. Arguably, uncertainties are often epistemic when first approached, reducible to some finite level where the remainder, if still significant, must be treated as aleatory.

Uncertainties related to the physical instrumentation can be regarded as mainly epistemic, except for the interrogator to some extent. The basic principle behind Fibre Bragg Gratings is uncomplicated in that characteristic wavelength changes with fibre length. The interrogator is, however, a sophisticated instrument, its processes subject to some finite uncertainty. For the overall physical implementation, uncertainties are largely related to the quality of the installation. Optical fibres must be treated with care and

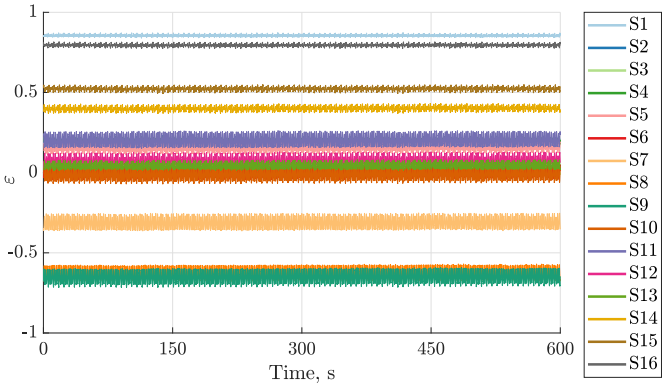

(a) Static and dynamic range for strain time series S1-S16 for a single 10-minute period

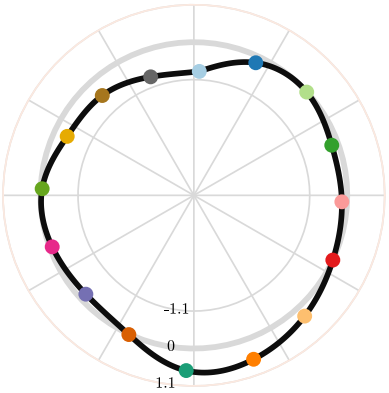

(b) Polar plot of S1-S16 mean values illustrating exaggerated static transverse deflection

Fig. 5. Typical S1–S16 strain time series and static deflection shape.

routed and protected to avoid attenuation in the optical path that might compromise bandwidth. As with strain sensors in general, correct alignment and proper bonding to the substrate must be ensured.

The simplified mathematical models used for data processing also constitute an epistemic uncertainty. Both the conversion of wavelength to strain and the separation of thermal strain and mechanical strain depend on temperature. Using a linearly interpolated temperature between two measurements is a simplification based on an assumed spatial distribution. Again, this simplification and thus uncertainty mostly affect the static part of the strain, because of the system thermal time constants. Presenting data as displacement instead of strain also introduces model uncertainty; considering that both strain and deflection are continuous and periodic, and that strain is the second order derivative of the deflection, the two quantities are spatially in phase, however, the amplitude of the deflection is uncertain.

None of the uncertainties mentioned so far are considered to invalidate a study of dynamic variation in strain or deflection. On an absolute scale, however, there is significant uncertainty related to the lack of knowledge on conditions during sensor installation. The state of absolute and distributed strain from bearing preload is not known, neither are the exact surface temperatures and temperature gradients in all parts of the bearings and surrounding structures. However, heating fans were used to control the air and bulk metal surface temperatures inside the nacelle to secure proper bonding and were left running over an ample period to allow the structure to soak the heat.

Bearing temperatures during operation have an element of aleatory uncertainty. The two temperature FBG sensors are placed at the top and bottom of the bearing, assuming that these are the locations of the highest and lowest temperatures. This might not be the case; the maximum and minimum temperatures could be in other circumferential positions, not necessarily diametrically opposite, and there could be several local maxima and minima. The spatial variation at any given time could be mapped but is likely to change with operational variables such as speed and load, tribological factors, and wear. Thus, temperatures *as modelled* could be represented by some distribution, or even better by pairing strain and temperature FBG sensors in every circumferential position. However, this would still leave the uncertainty related to bearing transverse temperature gradients.

Uncertainty related to any of the other measured quantities used in the analysis will not be assessed in detail. The wind speed measurements used stems from the anemometer that is part of the turbine's control and monitoring system. The anemometer is installed on the nacelle exterior in the wake of the rotor, and corrections are applied to approximate the speed from the incoming wind field.

The strain data, the operational data from the turbine and the wave buoy data are acquired in separate systems, meaning that they are not time stamped on the same clock. Care has been taken in ensuring that time series are aligned sufficiently not to introduce significant errors in the presented analyses.

4. Time-domain analysis

4.1. A single time-series and the static condition

The length of the recorded time series is 10 min, based on the criteria that approximately 100 rotations at rated speed are captured. Fig. 5(a) shows a representative time series of strains S1–S16, recorded at operation around rated wind speed, and referenced to the sensor installation condition, i.e. nacelle without rotor. Two aspects are immediately evident; First, the maximum static offset between individual time series is far greater than the maximum amplitude of any of the series. Secondly, the amplitude of the time series indicate that strain dynamics is most pronounced in the bearing lower half.

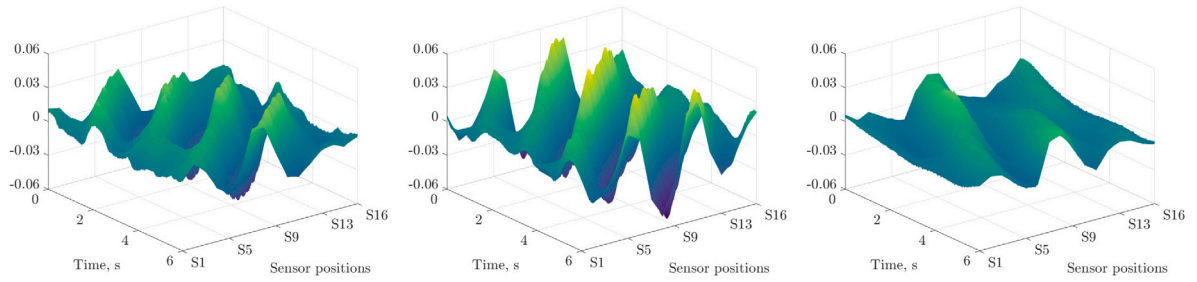

(a) Bending strain, v_W = 20.79 m/s (b) Bending strain, v_W = 9.85 m/s (c) Bending strain, v_W = 3.48 m/s

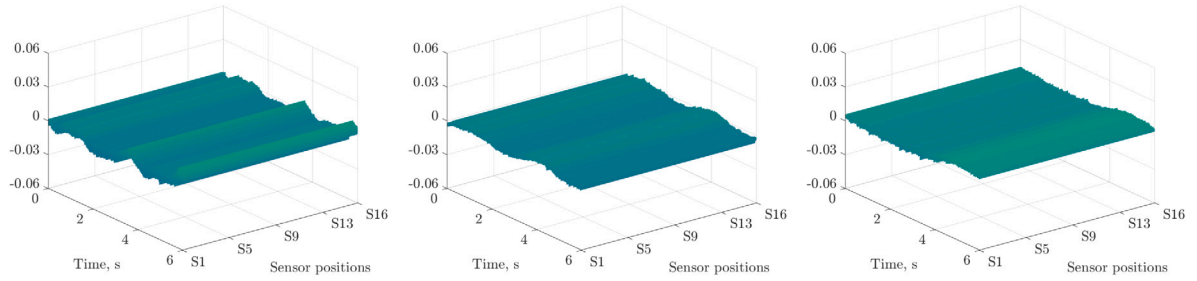

(d) Membrane strain, v_W = 20.79 m/s (e) Membrane strain, v_W = 9.85 m/s (f) Membrane strain, v_W = 3.48 m/s

Fig. 6. Dynamic bending strain and dynamic membrane strain at three different wind speeds, v_w.

The static offsets of the measured values in the top and bottom half of the bearing are fairly symmetrically placed about zero. Given that the measurements are on the stationary bearing parts, that is, on the receiving end of forces transmitted through the rollers, there is virtually no circumferential coupling, and the distribution is bound to mostly represent bending. The signs of the strains indicate inward bending of the bearing top half and outward bending of the bearing lower half. Fig. 5(b) shows a reversed-sign, polar plot of the static strain with coloured markers corresponding to the time series in Fig. 5(a). A cubic spline fitted black curve gives an exaggerated picture of the deformation, believed to be largely caused by the downward bending moment from gravity acting on the overhung rotor. The fit is made using overlapping points to ensure continuity at the joint.

4.2. Bending strain and membrane strain

According to the simplified theory presented in Section 3.3, strain is separable in membrane strain and bending strain. The membrane strain is taken as the spatial average over the circumference of the bearing at each time step. Figs. 6(a–c) show the dynamic bending strain and Figs. 6(d–f) show the dynamic membrane strain as surface plots over time and unfolded circumferential positions, with static content removed. Having identical scales, the plots show that the amplitude of the bending strain is approximately one order of magnitude larger that of the membrane strain.

The timescale in the figures equals the duration of one rotation at rated speed, representing only one hundredth of a time series. The spatial wave number and the oblique angle of the waviness clearly show how the bending strain is dominated by bending moments from the three blades, transmitted through the hub to the bearing.

Figs. 6(a, d) show operation at high wind speed, and Figs. 6(b, e) show operation at rated wind speed. Bending strain amplitude is markedly larger at operation around rated wind speed. As bending strain decreases with increasing wind speed above rated, and thus with lower thrust, it is evident that the bending strain in the bearing is the result of hub deflection from both in-plane and out-of-plane bending moments from the blades.

In Figs. 6(c, f), showing operation below rated wind speed, the smaller oblique angle of the waviness is the result of lower rotor speed.

Membrane strain fluctuation is expected to largely follow axial force or thrust. This is according to the assumption that the cause is a combination of net circumferential strain change from hub compression or expansion resulting from out-of-plane bending moments from the blades, and the coupling between axial and radial loads because of the locating function of the main bearings. As the plots in Fig. 6 only capture short-period changes, there is no contradiction in the fact that the high-wind and high-turbulence condition in Fig. 6(d) shows a slightly larger membrane strain amplitude than the high-thrust condition in Fig. 6(e).

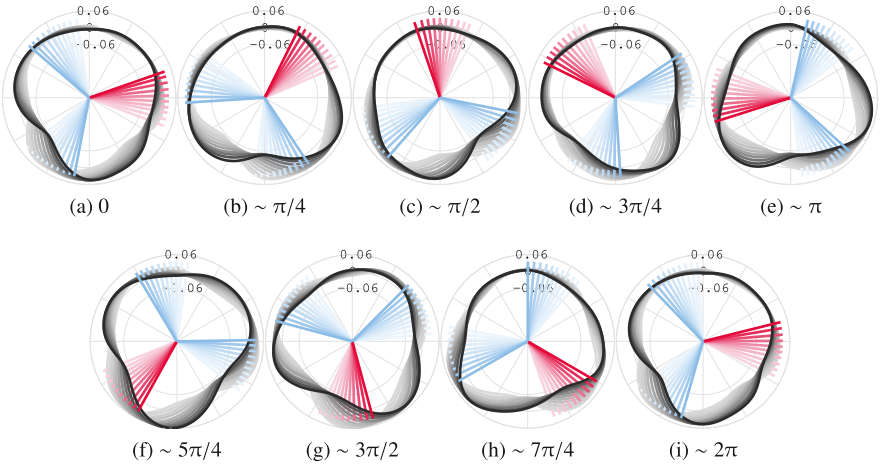

Fig. 7. Exaggerated bending deflection through one full rotation, seen in aft-fore direction.

4.3. Visualization of dynamic deflection

Plotting the strain in polar coordinates as in Fig. 5(b) gives a good visualization of bearing in-plane deflection. Fig. 7 shows similar, exaggerated plots of the dynamic deflection only, through approximately one full rotation of the shaft, pictured in nine frames, (a) to (i), taken at equidistant times. Direction of rotation is counter-clockwise, as viewed along the shaft in the aft-fore direction. Trailing shadows fading in backwards direction show the change from one frame to the next. Rotor position is also shown in the plot, the radial lines corresponding to blade root centre positions and the red lines indicating a reference blade.

In practice, the colloquial term 'non-torque loads' is related to the generalization of bearings as 5-DOF systems, as torque corresponds to the omitted, sixth DOF. Although the analysis presented here is not concerned with the net torque *per se*, the cross section will deform under differential bending moments from the blades on the hub, both in-plane and out-of-plane. These arise from varying aerodynamic forces (lift and drag), acting both in-plane and out-of-plane, and from gravity, acting mostly in-plane (depending, of course, on the static rotor axis tilt angle and rotor coning angle, as well as dynamic deflection).

In Fig. 7, a rotating triangular or 'third order' pattern from the blade bending moments is visible, indicating that deformation from differential blade bending moments occur. Three aspects can explain why the largest deflections take place in the lower half of the bearing. First, the upper part of the bearing ring is more constrained because of the larger static contact forces from the rollers in this area. Secondly, the hub will see a 3P differential bending moment from gravity acting on blades positioned off the vertical axis on both sides of the hub, 'folding' the underside of the hub. Lastly, the tower passing will largely affect the aerodynamic forces on the blade. Just by looking at Fig. 7, it is difficult to assess to what extent the differential bending moment from tower passing exacerbates the hub 'folding' bending moments from gravity or vice versa. It is, however, possible to observe a slight non-symmetry in the deformation across the vertical axis, resulting from the sum and difference, respectively, between torque-generating bending moments and gravity bending moments.

4.4. Environmental loads and floater motion

The strain data are recorded as ten-minute time series once per hour in 24-hour clusters, meaning that each cluster contains 24 ten-minute time series. The time interval between recorded clusters range from one week to several months.

Two clusters, representative of typical weather conditions on the site in the North Sea, have been selected for the analysis in this paper. Cluster 1 represents variable environmental conditions under operation above rated wind speed, and Cluster 2 captures operation both above and below rated wind speed.

The first and the last Cluster 1 time series were recorded on 2019-08-21, 16:33:28–16:43:28 Central European Time (CET) and on 2019-08-22, 15:33:28–15:43:28 CET. The first and the last Cluster 2 time series were recorded on 2019-10-28, 16:45:00–16:55:00 CET and on 2019-10-29, 15:45:00–15:55:00 CET. For reasons of one turbine shutdown and three instances of aborted data acquisition, four of the times series in Cluster 2 are truncated, the shortest containing a little more than five minutes of data.

Sea state data from the wave buoy are available as spectral significant wave height H_{m0} and peak wave period T_p based on ten-minute time series. These are plotted together with ten-minute mean values for wind speed, floater pitch angle, bending strain and membrane strain in Figs. 8 and 9.

Each of the selected clusters enable comparison of responses at different environmental loads while representing otherwise unchanged turbine condition and configuration. The disadvantage can be that they as clusters do not represent the most consistently stationary conditions within the ten-minute windows. Such statistical uncertainties can be reduced by performing more measurements in different environmental conditions over time. As an example, Fig. 10(a) shows how wind speed time series 17 has more

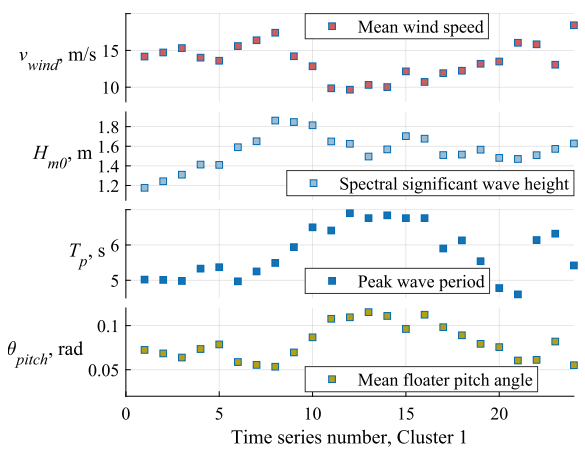

(a) Mean wind speed, spectral significant wave height, peak wave period and mean floater pitch angle

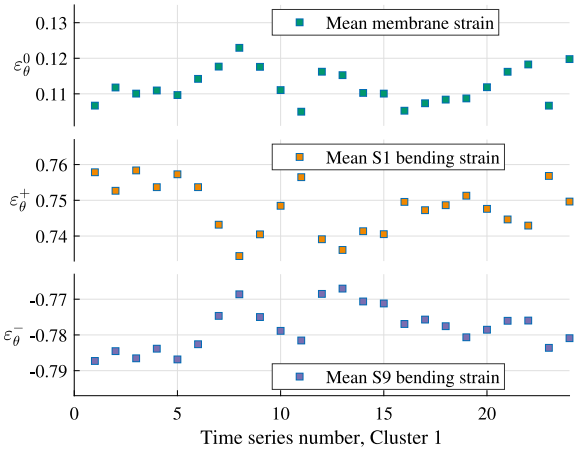

(b) Mean values membrane strain and S1 and S9 bending strains

Fig. 8. Cluster 1, environmental variables and strains, ten-minute statistical values.

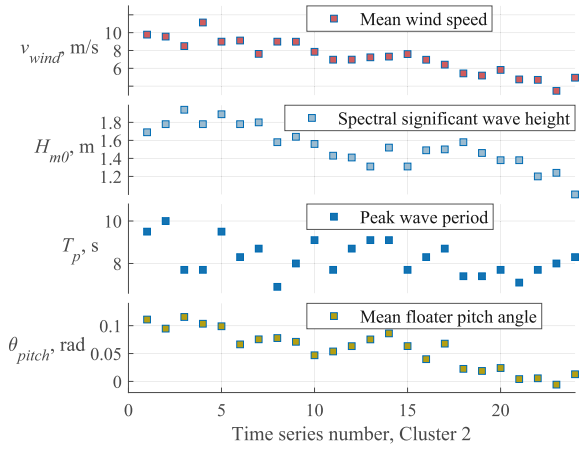

(a) Mean wind speed, spectral significant wave height, peak wave period and mean floater pitch angle

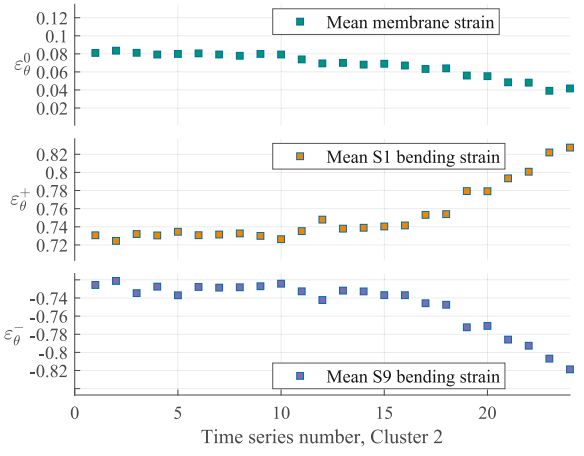

(b) Mean values, membrane strain and S1 and S9 bending strains

Fig. 9. Cluster 2, environmental variables and strains, ten-minute statistical values.

slow-varying content than time series 7 in Cluster 1. Fig. 10(b) demonstrates how the slow-varying content of the wind speed is reflected in the corresponding floater pitch angle.

Wind speed spectra for Cluster 1 are shown in Fig. 11, where it can be seen that most of the energy is contained in the slow-varying content, showing as a line of peaks close to zero frequency across the spectra.

Figs. 12 and 13 show floater pitch and roll angle spectra for Cluster 1. Each figure is split into two subfigures (a) and (b) along the frequency axis, and the reason is adaptation to the approximately two orders of magnitude difference between the energy content of the response in the two parts of the frequency range. As expected, responses appear at pitch and roll natural frequencies, ω_{0pitch} and ω_{0roll}, indicated in Figs. 12(a) and 13(a), and at $\frac{1}{T_p}$, indicated in Figs. 12(b) and 13(b). Furthermore, as expected, the slow-varying content of the wind speed appear as low-frequency content in the pitch angle, but not in the roll angle.

In Figs. 8(b) and 9(b), bending strain S1 and S9 mean values are plotted against separate y-axes with different signs. The consistently opposite behaviour of S1 and S9 is indicative of changes in vertical bending moment with both wind shear and net wind speed. The net wind speed contribution is resulting from the initially tilted rotor angle and added floater pitch angle, and evident because of the clear peak as wind speed approaches rated from above. Membrane strain mean values are also plotted against a separate y-axis and is thrust driven as expected. Note the positive axis; because of the bearing geometry, increased axial force adds compressive strain in the stationary ring that the force is shifted towards. As thrust is shifting axial load away from the bearing ring with instrumentation, the increase in membrane strain with increasing thrust is consistent with relief of compressive preload.

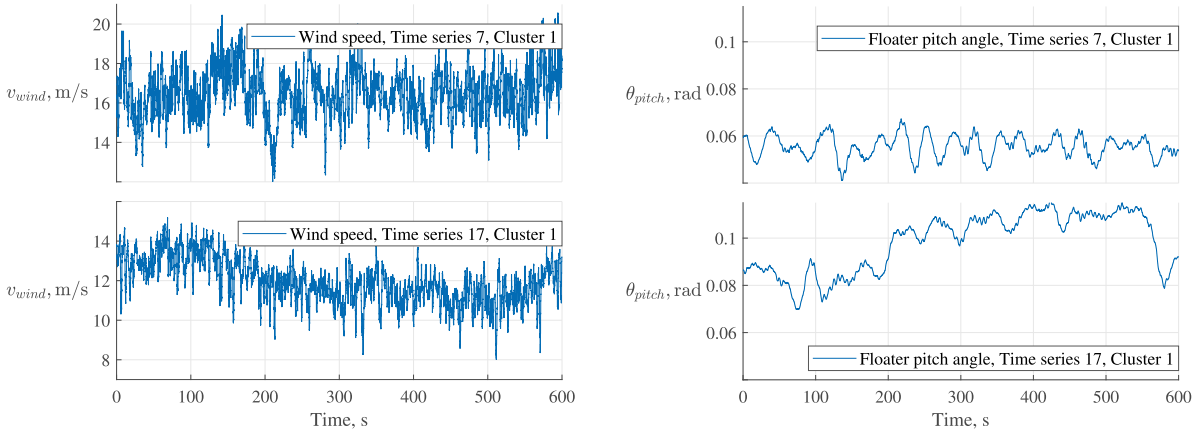

(a) Wind speed time series 7 and 17, Cluster 1

(b) Pitch angle time series 7 and 17, Cluster 1

Fig. 10. Cluster 1 — Wind speed and floater pitch motion time series.

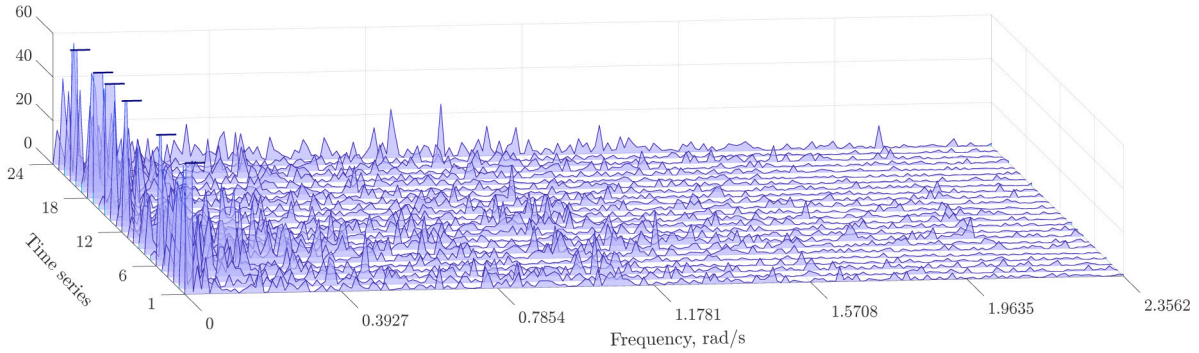

Fig. 11. Wind speed spectra, 0–2.3562 rad/s, per hourly ten-minute time series, chronological order, Cluster 1.

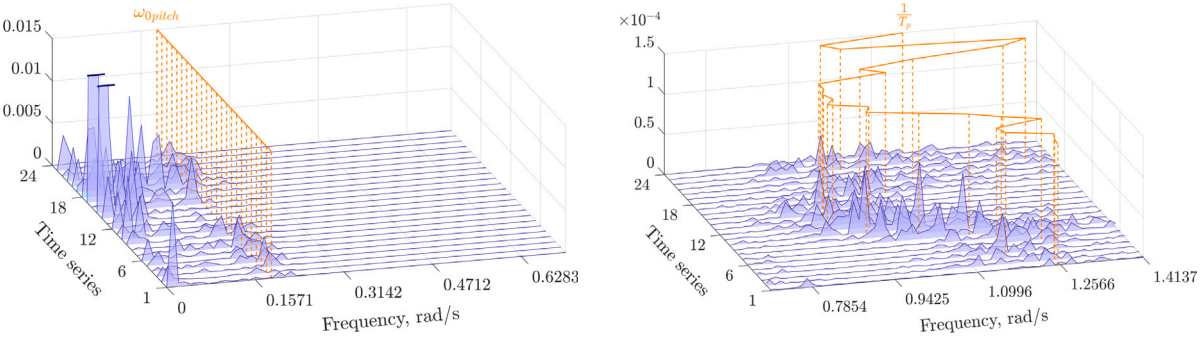

(a) Floater pitch angle, 0-0.7069 rad/s

(b) Floater pitch angle, 0.7069-1.4137 rad/s

Fig. 12. Cluster 1, floating turbine pitch angle spectra. Note the two orders of magnitude difference between the vertical scales in Figs. (a) and (b) and similarly between the responses at pitch natural frequency ω_{0pitch} and wave frequency $\frac{1}{T_p}$.

5. Frequency analysis

5.1. Low-frequency excitation and quasi-static response

The ratio of strain amplitudes to static strain levels has already been described in Section 4.1. The bearing vibrations with the highest energy are expected to occur at low frequencies. With respect to the bearing subsystem, these represent quasi-static responses. The main sources of low-frequency excitation are environmental loads from wind and waves, rotordynamic loads and

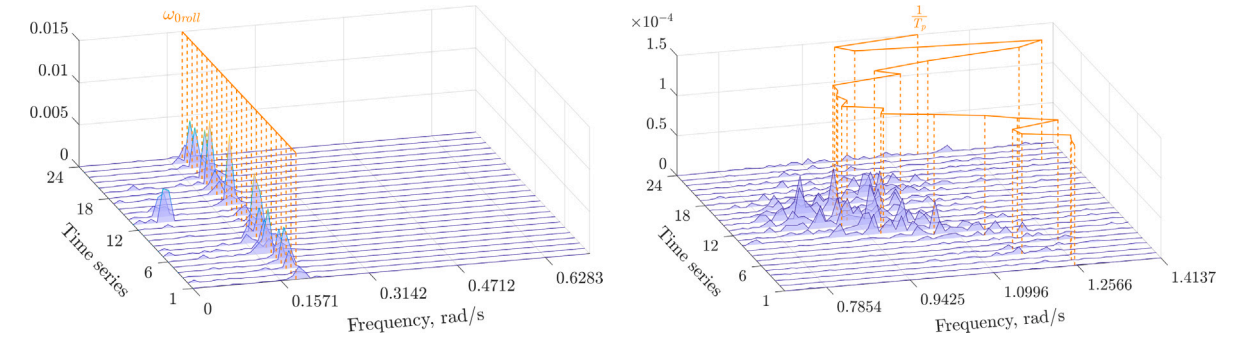

(a) Floater role angle, 0-0.7069 rad/s (b) Floater role angle, 0.7069-1.4137 rad/s

Fig. 13. Cluster 1, floating turbine roll angle spectra. Note the two orders of magnitude difference between the vertical scales in Figs. (a) and (b) and similarly between the responses at roll natural frequency ω_{0roll} and wave frequency $\frac{1}{T_p}$.

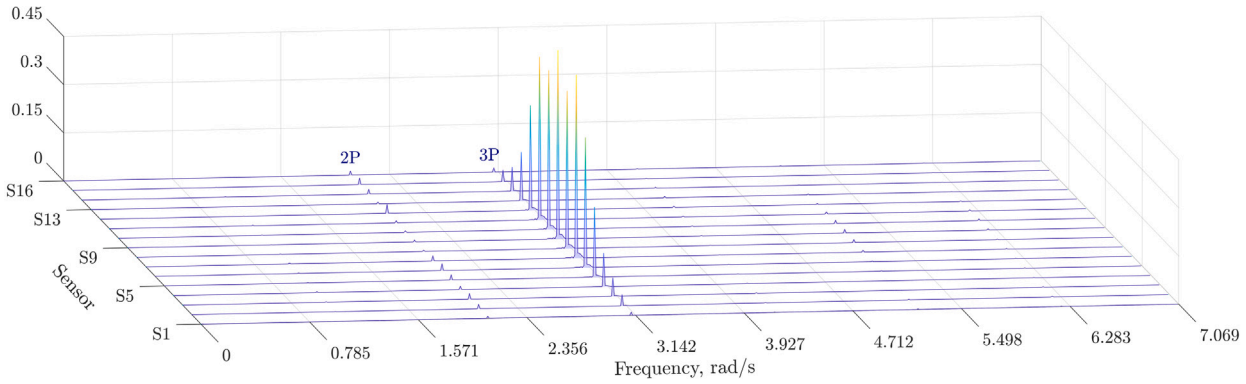

Fig. 14. Bending strain spectra, 0–7.069 rad/s, across sensor positions.

cyclic wind and gravity loads as caused by rotation. The anemometer providing wind speed measurement has a sampling rate of approximately 5 Hz. Most of the energy, however, lie below 0.5 Hz (3.1416 rad/s). From the wave buoy, spectral significant wave height H_{m0} and peak wave period T_p are available for the ten-minute time series. The rotational speed is approximately 10 rpm at rated power, and the corresponding 1P and 3P excitation frequencies are 0.167 Hz (1.047 rad/s) and 0.5 Hz (3.1416 rad/s).

The ten-minute time series are assumed to be stationary processes. Low-frequency spectra are generated using a single window to obtain the highest possible frequency resolution. Thus, $2500 \times 60 \times 10$ samples in 2500 Hz gives 0.00167 Hz bins.

Sensitivity to roller passing in the bearing is verified, but details regarding frequency and amplitude will not be discussed in this paper.

5.2. Low-frequency spatial response

Fig. 14 shows low-frequency spectra of the bending strain in each of the 16 sensor positions, arranged in a waterfall plot. The spectra are based on the same representative time series from operation around rated wind speed as used previously. It complements the observations made in Section 4.3, showing that 3P vibrations are totally dominant with the largest magnitudes localized in the lower half of the bearing. Barely visible in the same plot are peaks at 2P and 5P.

Fig. 15 is Fig. 14 zoomed in on the magnitude. Horizontal crossbars indicate curve clipping. Here, small peaks emerge also at 1P, 4P and 6P. Thus, all peaks appear to align with the excitation frequencies 1P and 3P and combinations or multiples thereof. 3P is inherent in the design. 1P is physical, as only a perfect rotor would be free of imbalance forces, and that is hardly achievable. Whereas the 3P vibration shows a clear first-order magnitude distribution over the positions, the 2P and 5P peaks show opposing, singly symmetric second-order distributions.

5.3. Bending strain load dependence

Fig. 16 shows a waterfall plot of low-frequency bending strain spectra, this time for the single sensor position S9, for each of the different time series in Cluster 1. As already stated, Cluster 1 represents operation above rated wind speed, where the rotational speed is close to constant. By comparison with Fig. 8 it is seen that the magnitude of the 3P response varies oppositely with wind

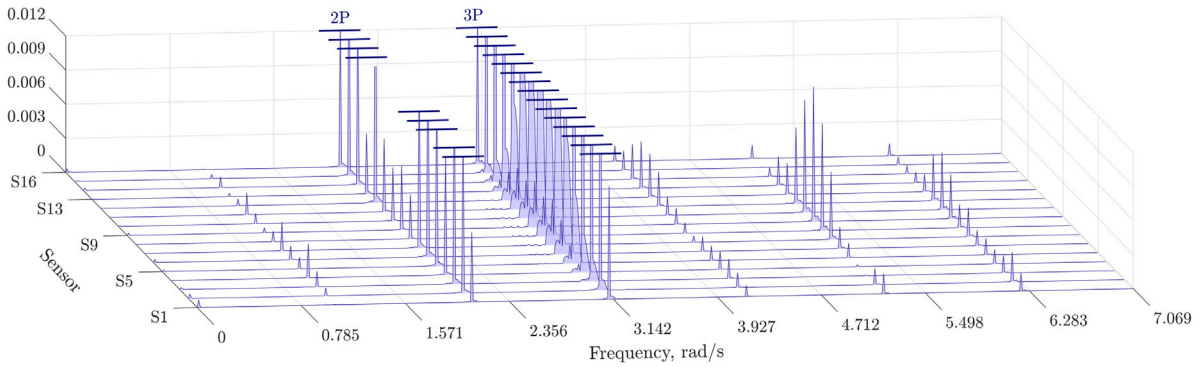

Fig. 15. Bending strain spectra, 0–7.069 rad/s, across sensor positions, zoomed in on magnitude.

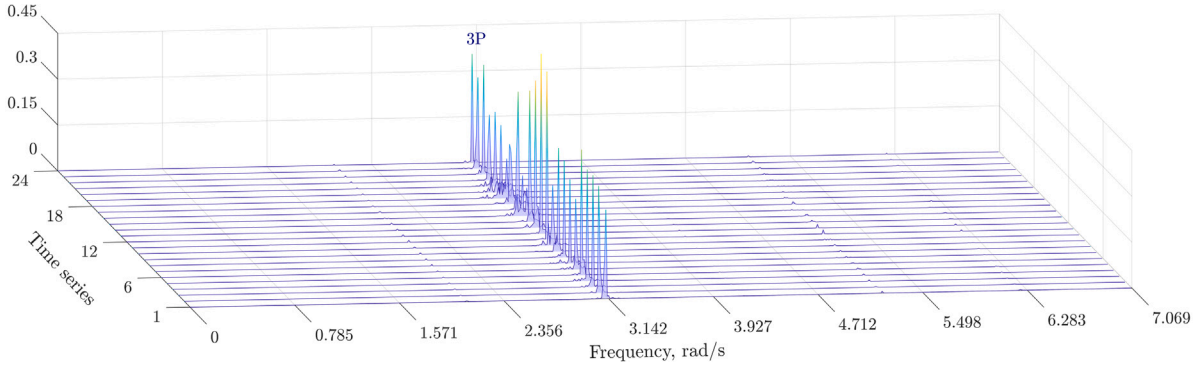

Fig. 16. S9 bending strain spectra, 0–7.069 rad/s, per hourly ten-minute time series, chronological order, Cluster 1.

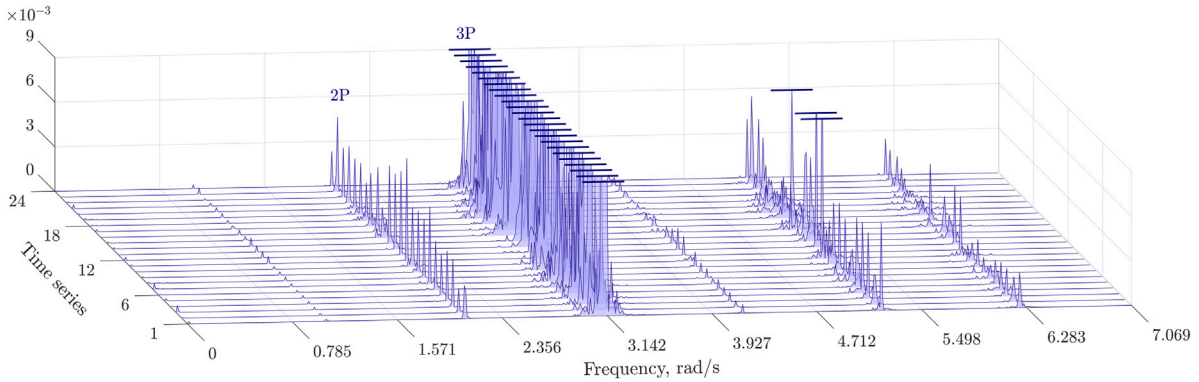

Fig. 17. S9 bending strain spectra, 0–7.069 rad/s, per hourly ten-minute time series, chronological order, Cluster 1, zoomed in on magnitude.

speed, peaking with maximum thrust around rated wind speed. Thus, it seems evident that aerodynamic forces, modulated by rotation through wind shear and tower shadow and causing cyclic differences between out-of-plane blade bending moments, form part of the 3P excitation. Interestingly, the magnitude appears to decrease rapidly with decreasing thrust and then increase again with increasing wind speed before levelling out. This indicates that the aerodynamic element of the 3P excitation is a combination of in-plane and out-of-plane bending, dependent on the angle of attack of the tower shadow.

Fig. 17 zooms in on the magnitude of the spectra in Fig. 16 and shows smaller peaks lining up across the spectra at 1P intervals. The scaling between the peaks seems fairly consistent across the spectra, that is, the ridges follow the same relation with wind speed as the dominant 3P response.

Figs. 18 and 19 show Cluster 2 spectra in the same manner as Figs. 16 and 17 show Cluster 1 spectra. Wind speed varies from above-rated down to almost cut-in. As already observed from the time-domain analysis and Fig. 6, the magnitude and frequency of the 3P response scale with wind speed and rotational speed. The drastic reduction at low wind speeds is interesting and indicates

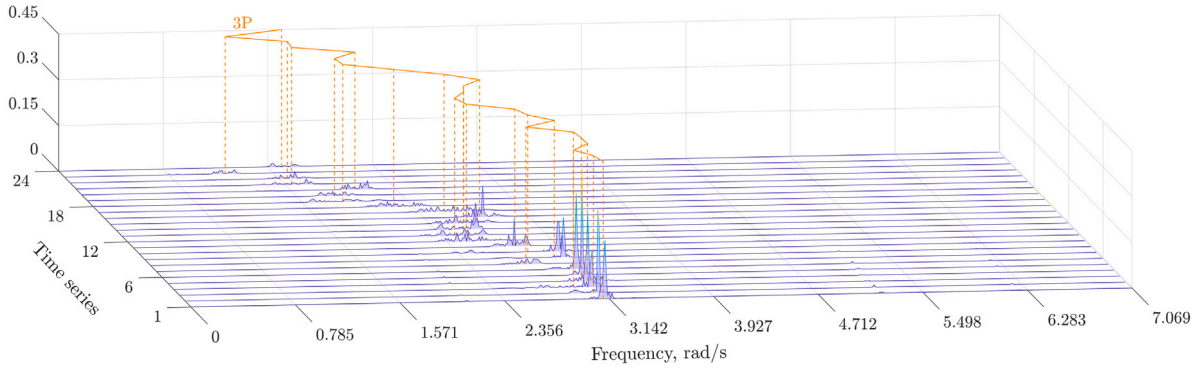

Fig. 18. S9 bending strain spectra, 0–7.069 rad/s, per hourly ten-minute time series, chronological order, Cluster 2.

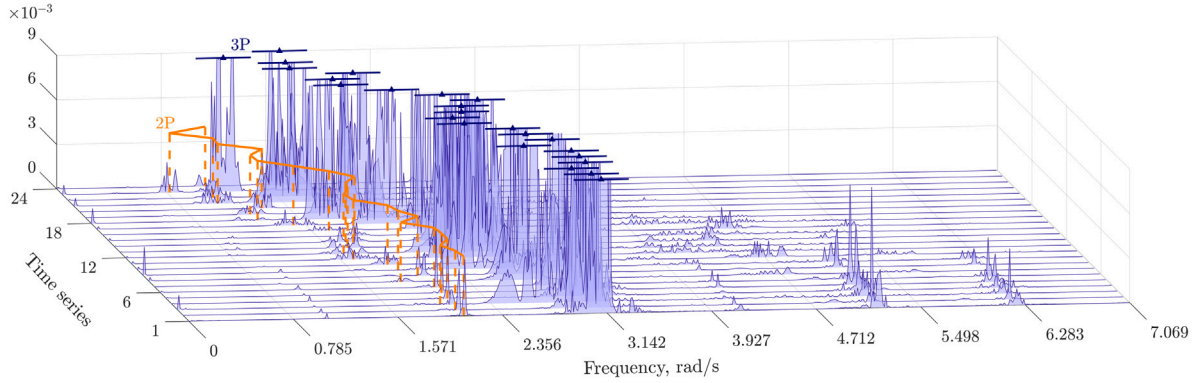

Fig. 19. S9 bending strain spectra, 0–7.069 rad/s, per hourly ten-minute time series, chronological order, Cluster 2, zoomed in on magnitude.

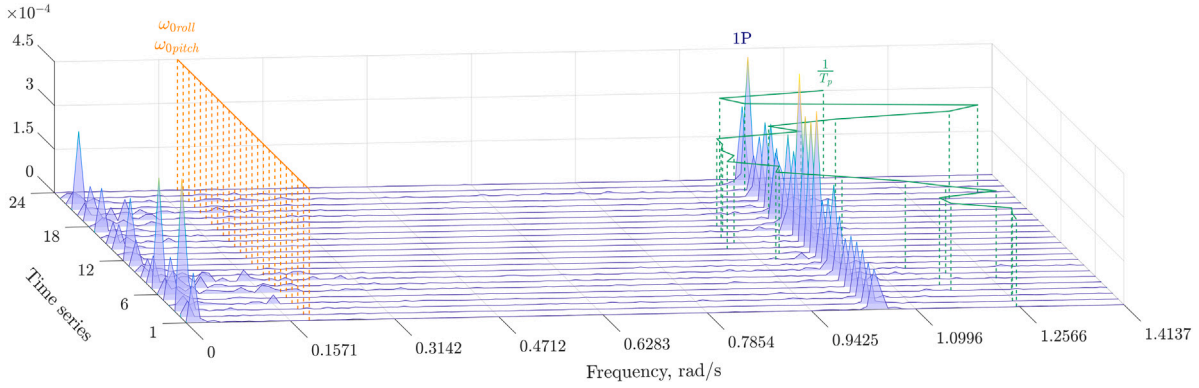

Fig. 20. S9 bending strain spectra, 0–1.4137 rad/s, per hourly ten-minute time series, chronological order, Cluster 1.

that gravity loads have little effect on the 3P excitation. While possibly also scaling with rotational speed, the smaller magnitudes of the 2P peaks seem less affected by the wind speed reduction.

Fig. 20 zooms further in on the magnitude as well as on the frequency range of the Cluster 1 spectra in Figs. 16 and 17, showing the 1P response barely visible in Fig. 17 and some slightly smaller slow-varying content. The floating turbine's almost identical natural frequencies in pitch and roll, ω_{0pitch} and ω_{0roll}, and the inverse of the peak wave period, $\frac{1}{T_p}$, are indicated in the figure, however, no responses can be observed at these frequencies.

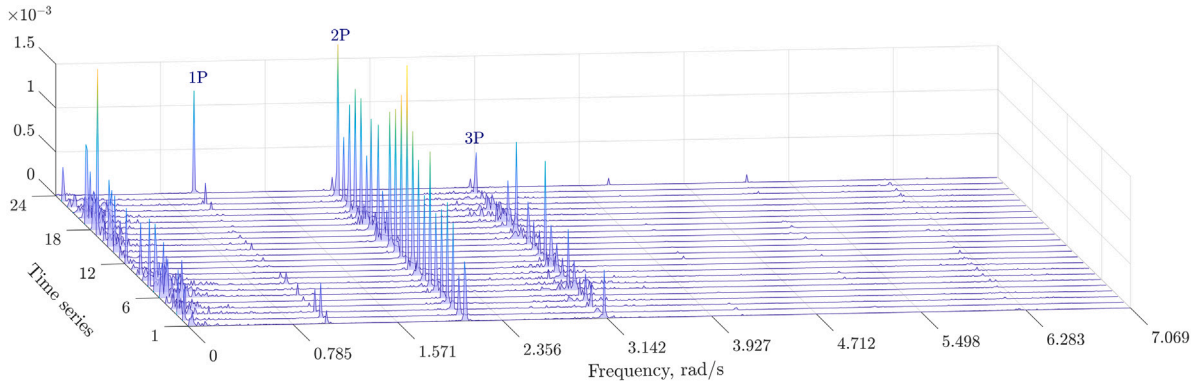

Fig. 21. Membrane strain spectra, 0–7.069 rad/s, per hourly ten-minute time series, chronological order, Cluster 1.

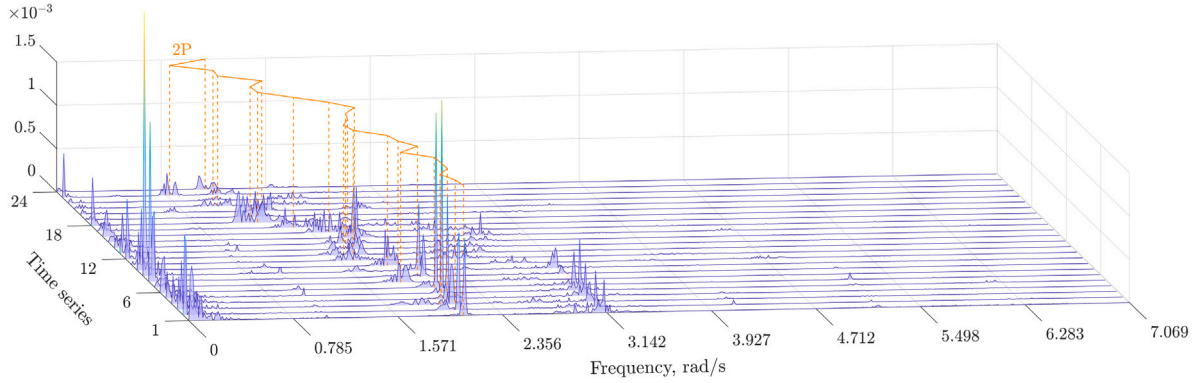

Fig. 22. Membrane strain spectra, 0–7.069 rad/s, per hourly ten-minute time series, chronological order, Cluster 2.

5.4. Membrane strain load dependence

The membrane strain has much lower amplitudes than the bending strain. Waterfall plots for the membrane strain for Clusters 1 and 2 are presented in Figs. 21 and 22, with even smaller magnitude scales than the zoomed-in bending strain plots in Figs. 17 and 19. Immediately apparent is the low 3P energy content, which does make sense; differential bending moments in the blades mostly show up as local bending in the bearing, as already seen. The domination of the 2P content is more surprising. In Fig. 21, the 2P membrane strain response strongly resembles the 2P bending strain response in Fig. 17. Comparing for Cluster 2 in Figs. 19 and 22, there seem to be larger differences in magnitude between bending strain and membrane strain 2P responses below rated wind speed. Figs. 21 and 22 show that slow-varying responses are largest around rated wind speed, or maximum thrust, where they have the same order of magnitude as the 2P response.

Fig. 23 zooms further in on the magnitude as well as on the frequency range of the spectra in Fig. 21, showing Cluster 1 membrane strain spectra on the same scales as used for Cluster 1 bending strain spectra in Fig. 20. By comparing Figs. 20 and 23, several aspects can be observed. First, the 1P membrane strain responses have approximately the same order of magnitude as the 1P bending strain responses, however, they appear to show a slightly opposite trend across the time series. Secondly, the slow-varying responses are larger for the membrane strain than for the bending strain. Thirdly, unlike the bending strain, the membrane strain shows a small response at the floating turbine's natural frequencies in pitch and roll, ω_{0pitch} and ω_{0roll}. Lastly, also unlike the bending strain, the membrane strain fairly consistently shows a response at close to the inverse of the peak wave period $\frac{1}{T_p}$, although very small.

5.5. Higher-frequency dynamic response

Figs. 24 to 27 show different waterfall plots of strain spectra up to 1250 Hz, which is the Nyquist frequency corresponding to the 2500 Hz sampling rate available when using all sensors. A lower frequency resolution of 0.833 Hz per bin is used in these plots, also lowering the magnitude of the peaks. Most of the energy lies in the low-frequency end of the spectra, where the steeply rising curves are clipped as indicated by small horizontal bars. Although low in energy content, peaks of different magnitude are present throughout the entire spectra.

Figs. 24 and 25 show waterfall plots of S9 bending strain spectra for the time series in Clusters 1 and 2. Zoomed in on the spectral content in the 125–1250 Hz range, these waterfall plots show differences in the baseline appearance between the two clusters, not

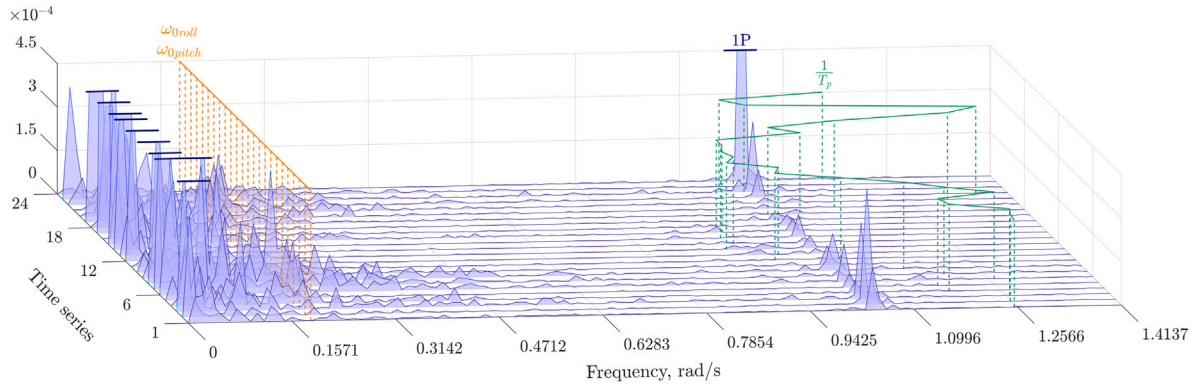

Fig. 23. Membrane strain spectra, 0–1.4137 rad/s, per hourly ten-minute time series, chronological order, Cluster 1.

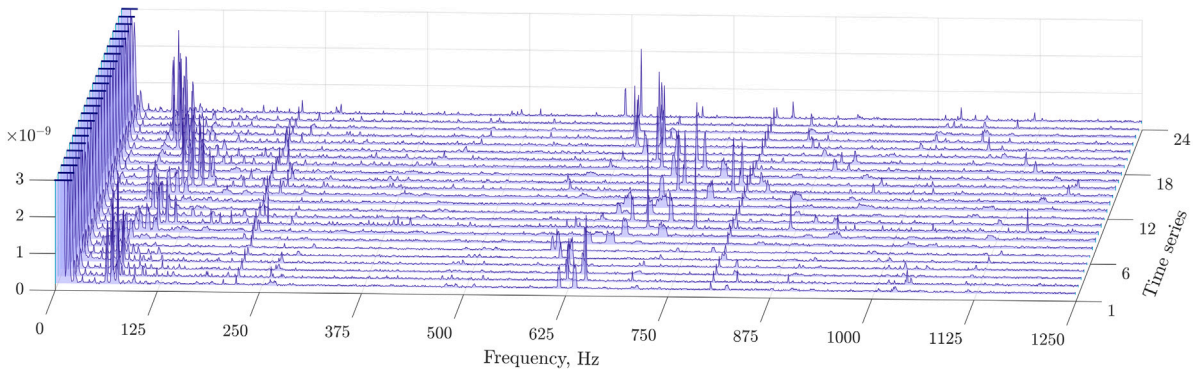

Fig. 24. S9 bending strain spectra, 0–1250 Hz, per hourly ten-minute time series, Cluster 1.

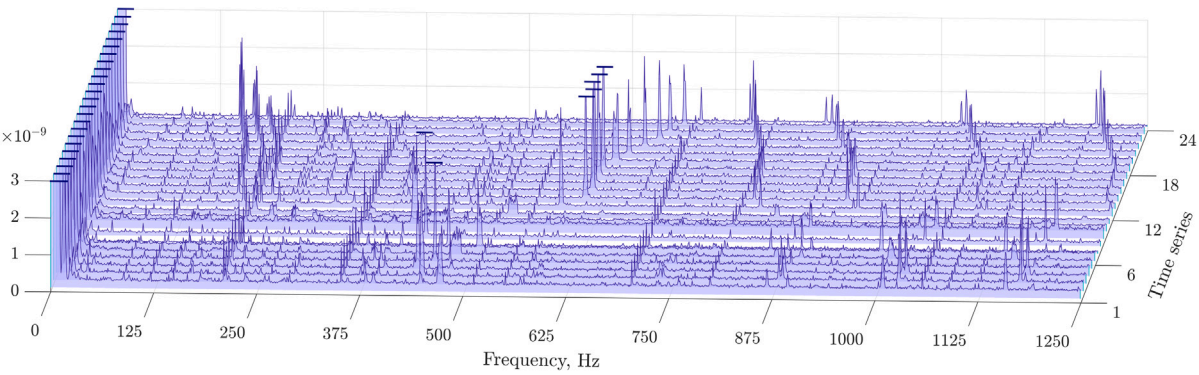

Fig. 25. S9 bending strain spectra, 0–1250 Hz, per hourly ten-minute time series, Cluster 2.

readily attributable to any known changes in system characteristics or excitation. The ten weeks between Cluster 1 and Cluster 2 represent only a small fraction of the turbine's design life, thus, any significant degradation or change in system characteristics would not be expected. However, the low energy content and the nonlinear bearing characteristics may point to even minor changes in the tribological conditions. A possible cause could be small changes in the lubrication, affecting both stiffness and damping in the bearing, over the ten weeks between Cluster 1 and Cluster 2. Across the spectra, peaks form bands whose frequencies are either constant or varying expressly with thrust. The dependencies are mostly such that frequency increases with increasing thrust, and thus, intuitively, with the net stiffening of the whole bearing assembly from balancing of the axial force. However, opposite trends are also observed.

Figs. 26 and 27 show waterfall plots of spectra of membrane strain per time series in Clusters 1 and 2. Similarly to the bending moment responses in Figs. 24 and 25, peaks form bands with frequency dependent on thrust.

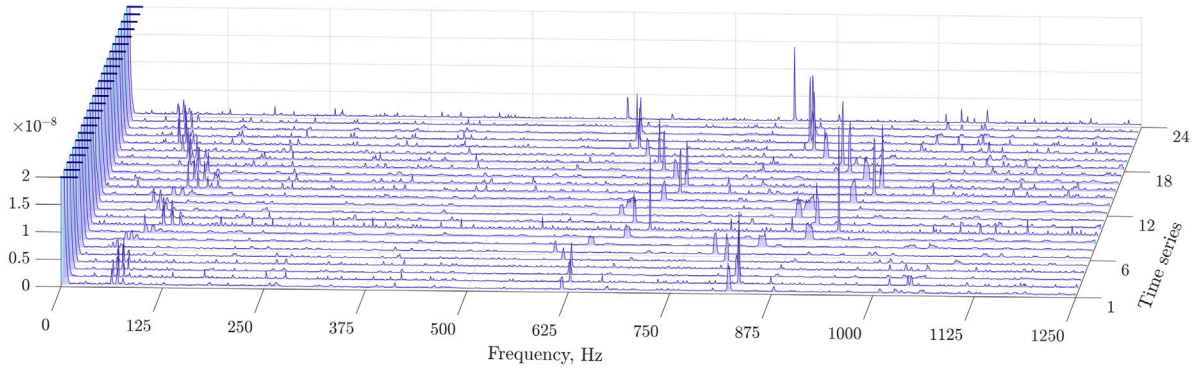

Fig. 26. Membrane strain spectra, 0–1250 Hz, per hourly ten-minute time series, Cluster 1.

Fig. 28 is a bit crowded, showing an overlay of four waterfall plots across the sensor positions, each with a different fill colour. The waterfalls represent the bending moment spectra belonging to four different time series in Cluster 1. Interestingly, the plot shows what appears to be bifurcations; the single band of peaks appearing at approximately 1070 Hz for time series eight seems to split into two bands in the other time series, the largest spacing between corresponding frequencies seen for time series six.

The bearings and surrounding structures are essentially rotationally symmetric, and assuming mode shapes for natural, force free vibrations is fairly straightforward. Assessing the natural frequencies is more difficult because of the nonlinear stiffness of the bearing and, thus, the dependence on load and preload.

The first transverse (bending) natural modes of the stationary bearing ring are roughly estimated to have frequencies at least two orders of magnitude higher than 1P and 3P, possibly appearing in the spectra. The number of measurement positions is grossly redundant for identification of lower-order natural modes. By trading spatial bandwidth for temporal bandwidth, as described in Section 3.1, vibrations are also identified at higher frequencies than 1250 Hz. Possibly linked to electrical excitation, these vibrations will not be treated here.

Operational Modal Analysis (OMA) methods have been briefly employed to interpret the higher-frequency bending strain responses. The task is challenging because of the relatively low-energy content and the fact that these responses represent nonlinear behaviour and thus violates one of the basic assumptions behind OMA.

Contrary to bending strain, membrane strain leaves little ambiguity with respect to mode shapes as higher-order, natural extensional modes have frequencies well above 1250 Hz.

6. Discussion

We see that the stationary bearing ring undergoes fluctuating circumferential strain with amplitude approximately one order of magnitude smaller than the static bending strain caused by gravitational pull on the rotor. Further, as per our simplified mathematical model, the amplitude of the membrane strain fluctuation is approximately two orders of magnitude smaller than the amplitude of the largest bending strain fluctuation. The spatial difference in bending strain amplitude along the sensor array is also almost one order of magnitude, with the largest fluctuations occurring in the lower half of the bearing.

The fluctuating bending deflection is dominantly a quasi-static response to 3P excitation from differential bending moments between the blades, both in and out of the rotor plane. The bending moments are modulated as the blades pass through the wind shear and the tower shadow (both in-plane and out-of-plane) and rotation vary the angle of attack of gravity forces on the blades (mostly in-plane). The shown dependence of main bearing deflections on blade bending moments in the present turbine design strongly indicates that these moments constitute important load interfaces not only for the global turbine structure but also for the main bearing and drivetrain subsystem.

An interesting aspect of the analysis emerges in the frequency domain. We see that the rotational speed-dependent, low-frequency responses line up in orders of 1P. Besides the dominant 3P excitation there is also a small 1P excitation. This is intuitive; no physical rotating system is perfectly balanced. The presence of a 2P response inevitably leads to an assessment of possible 2P excitation sources; in rotordynamics typically caused by misalignment. In the present design, misalignment issues are neither a straightforward proposition nor can be completely excluded. Considering the highly nonlinear stiffness of the bearing, the 2P content is more likely a sideband resulting from the combination of 1P and 3P excitation. Interestingly, the 2P content is dominant in the membrane strain.

The similarity between bending strain 3P spectral content and membrane strain 2P spectral content in terms of wind speed and thrust dependence indicates a coupling between the two. A possible physical explanation is that membrane strain is not just the result of coupling between thrust and radial force because of the bearing geometry, but also in-plane extensional deflection of the hub and the rotating bearing ring related to the total out-of-plane bending of all three blades.

The wind speed spectra in Fig. 11 show that most of the energy in the wind lies below 2.3562 rad/s (0.375 Hz). In all figures showing strain spectra in the 0–7.069 rad/s (0–1.125 Hz) range, the only visible content, other than that close to the orders of P, are small bands close to zero frequency.

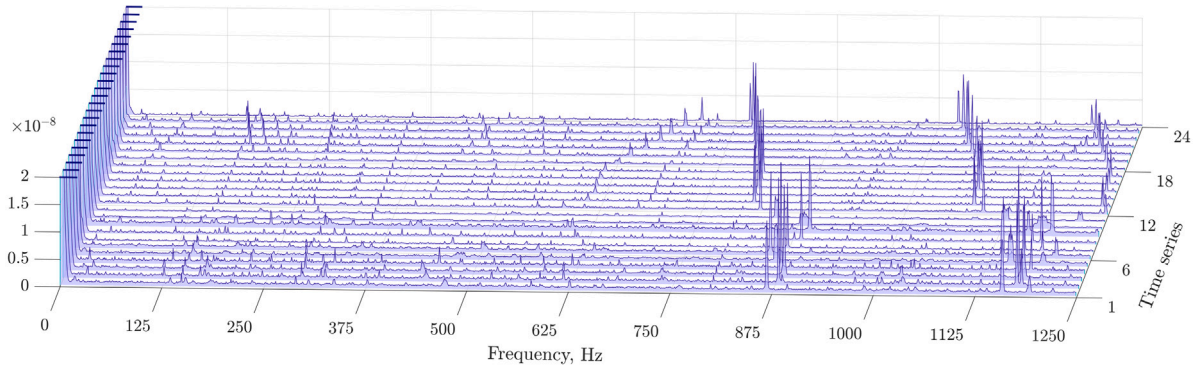

Fig. 27. Membrane strain spectra, 0–1250 Hz, per hourly ten-minute time series, Cluster 2.

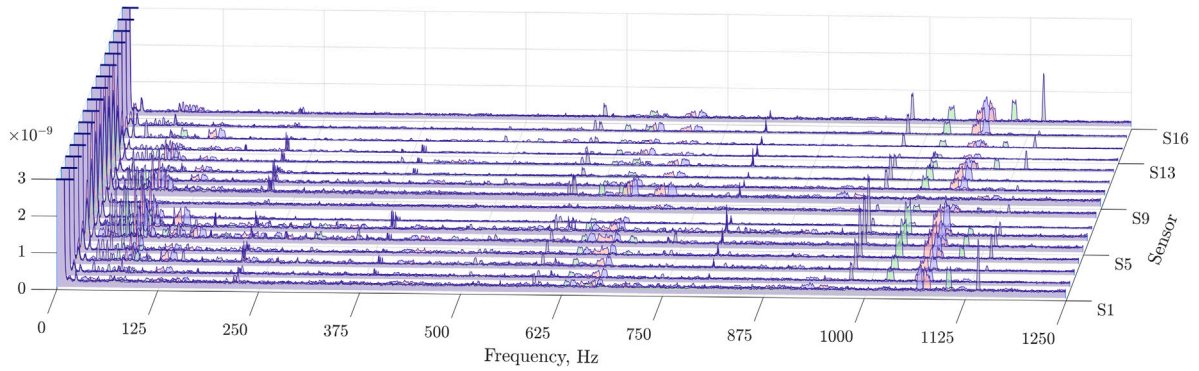

Fig. 28. Bending strain spectra, 0–1250 Hz, per sensor position for Cluster 1, time series 6 (grey), 7(green), 8(blue) and 12 (red). (For interpretation of thereferences to colour in this figure caption, the reader is referred to the web version of this article.).

In the zoomed-in view of the Cluster 1 membrane strain spectra in Fig. 23, the lowest-frequency content appears as a combination of the wind spectra in Fig. 11 and the floating turbine pitch angle spectra in Fig. 12(a). A small amplification can be observed close to the pitch natural frequency, approximately one order of magnitude smaller than the dominant 2P response. The pitch angle response at $\frac{1}{T_p}$ shown in Fig. 12(b) is barely visible in Fig. 23.

Using the same scales as Fig. 23, Fig. 20 shows that the magnitude of the low-frequency content is significantly lower in the bending strain than in the membrane strain. In both figures, a substantial part of the lowest-frequency content lines up across the spectra in the frequency bins next to zero frequency, mostly representing slow-varying response and non-stationarity in the ten-minute time series. In the membrane strain, these response peaks are smaller than, but the same order of magnitude as, the 2P response. In the bending strain, however, the difference between the slow-varying response and the dominant 3P response approaches three orders of magnitude.

7. Conclusion

Our experimental study based on circumferential strain measurements in the stationary ring of a main bearing in a floating offshore wind turbine shows that the contribution to fluctuating strain from in-plane bending deflection is two orders magnitude larger than the contribution from extensional deflection. The fluctuating in-plane bending deflection of the bearing ring is the result of cyclic variations in blade bending moments, both in and out of the rotor plane, as the turbine rotates. These variations are primarily driven by wind shear and tower shadow, and thus dependent on wind speed.

The fluctuating membrane strain appears to be the result of both axial load from thrust, because of the bearing and roller geometry, and radial loads on the rotating bearing ring related to the total out-of-plane bending of all three blades. The absolute contribution from fluctuating wind speed and floater pitch motion to low-frequency fluctuating strain is larger in the membrane strain than in the bending strain. Contributions from wave forces are negligible in both.

In the membrane strain, the low-frequency responses are smaller than, but the same order of magnitude as the dominant 2P response. It is not unexpected that the effects of floater motion come through in relation to axial load carrying in the main bearing in a floating wind turbine, however, assessing the relative importance on basis of the membrane strain is difficult, as the characteristics of the dominant 2P response is likely highly dependent on the drivetrain design.

Overall, considering that the total fluctuating strain is dominated by the intrinsic effects of blade bending moments at 3P frequency in these turbines, the relative effect of floater motion is very small.

It is demonstrated that the membrane strain and bending strain responses in the bearing stationary ring are affected by the nonlinear characteristics of the bearing. The magnitude of the sum- and difference frequencies at different orders of P are small compared to the dominant 3P bending strain. However, sum- and difference frequencies appear fundamental for the coupling between bending strain and membrane strain and the resulting, dominant 2P membrane strain response. This is an important result with respect to turbine modelling and simulation, where global structural analyses and local drivetrain analyses are frequently decoupled.

The results of our analyses imply that both the relative contribution of floater motion to bearing deflection and the importance of nonlinear effects are dependent on drivetrain design and thus indirectly on turbine size.

Declaration of competing interest

The authors declare that they have no known competing financial interests or personal relationships that could have appeared to influence the work reported in this paper.

Funding This work was supported by Equinor ASA; and the Research Council of Norway [project number 263819].

References

[1] Sieros G, Chaviaropoulos P, Sørensen JD, Bulder BH, Jamieson P. Upscaling wind turbines: theoretical and practical aspects and their impact on the cost of energy. Wind Energy 2012;15(1):3–17. http://dx.doi.org/10.1002/we.527, http://onlinelibrary.wiley.com/store/10.1002/we.527/asset/we527.pdf?v=1&t=iu5sxip4&s=80d6ab28d1e8f1a71c2753e9c8ac12edafc811b8.

[2] INNWIND - Innovative WInd Conversion Systems(10-20MW) for Offshore Applications, http://www.innwind.eu/.

[3] Stehouwer E, van Zinderen GJ. Conceptual nacelle designs of 10-20 MW wind turbines. In: INNWIND. Technical Report, 2016, Deliverable D3.41.

[4] Gaertner E, Rinker J, Sethuraman L, Zahle F, Anderson B, Barter G, et al. Definition of the IEA wind 15-megawatt offshore reference wind turbine, NREL/TP-5000-75698. Technical Report, Golden, CO: National Renewable Energy Laboratory; 2020, www.nrel.gov/publications.

[5] Smith EB. Design av nacelle for en 10 mw vindturbin (Ph.D. thesis), Institutt for produktutvikling og materialer, NTNU; 2012, p. 62, https://ntnuopen.ntnu.no/ntnu-xmlui/handle/11250/241691.

[6] Kabus S, Pedersen CBW. Optimal bearing housing designing using topology optimization. J Tribol 2012;134(2). http://dx.doi.org/10.1115/1.4005951, http://tribology.asmedigitalcollection.asme.org/data/journals/jotre9/28789/021102_1.pdf.

[7] Kabus S, Hansen MR, Mouritsen OØ. A new quasi-static multi-degree of freedom tapered roller bearing model to accurately consider non-hertzian contact pressures in time-domain simulations. Proc Inst Mech Eng K: J Multi-Body Dyn 2014;228(2):111–25. http://dx.doi.org/10.1177/1464419313513446, http://pik.sagepub.com/content/228/2/111.full.pdf.

[8] Dabrowski D, Natarajan A, Stehouwer E. Structural optimization of an innovative 10 MW wind turbine nacelle. In: EWEA 2015. European Wind Energy Association (EWEA); 2015.

[9] Dabrowski D, Natarajan A, Bulder BH, Bot ETG. Report on PI assessment of reduced tower top mass concepts. In: INNWIND. Technical Report, 2015, Deliverable D 1.31.

[10] Kock S, Jacobs G, Bosse D. Determination of wind turbine main bearing load distribution. J Phys Conf Ser 2019;1222:12030. http://dx.doi.org/10.1088/1742-6596/1222/1/012030.

[11] Peeters J, Vandepitte D, Sas P, Lammens S. Comparison of analysis techniques for the dynamic behaviour of an integrated drivetrain in a wind turbine. 2002, p. 1397–405.

[12] Schlecht B, Schulze T, Hähnel T. Multibody-system-simulation of drive trains in wind turbines. In: ISMA2004. 2004, p. 3953–67.

[13] Schlecht B, Rosenlöcher T, Hähnel T. Strategy for user orientated simulation of large drive trains to calculate realistic load conditions. In: ISMA2008. Vol. 4, Noise and Vibration Engineering, 23rd International Conference. (ISMA2008); 2008, p. 2129–41.

[14] Helsen J, Heirman G, Vandepitte D, Desmet W. The influence of flexibility within multibody modeling of multi-megawatt wind turbine gearboxes. In: ISMA2008. Vol. 4, 2008, p. 2045–71.

[15] Helsen J, Vanhollebeke F, Marrant B, Vandepitte D, Desmet W. Multibody modelling of varying complexity for modal behaviour analysis of wind turbine gearboxes. Renew Energy 2011;36(11):3098–113. http://dx.doi.org/10.1016/j.renene.2011.03.023, http://ac.els-cdn.com/S0960148111001376/1-s2.0-S0960148111001376-main.pdf?_tid=7cebaf5e-8c60-11e6-94f4-00000aab0f02&acdnat=1475825852_ae7fc3f7c9b42efb52aa311ac4488a14.

[16] Helsen J, Peeters P, Vanslambrouck K, Vanhollebeke F, Desmet W. The dynamic behavior induced by different wind turbine gearbox suspension methods assessed by means of the flexible multibody technique. Renew Energy 2014;69:336, http://www.sciencedirect.com/science/article/pii/S0960148114002006, http://ac.els-cdn.com/S0960148114002006/1-s2.0-S0960148114002006-main.pdf?_tid=4906f94c-8c5f-11e6-b705-00000aab0f02&acdnat=1475825335_f8c9fdb2e3e8f2ca5d7c70400421ee0a.

[17] Nejad AR, Guo Y, Gao Z, Moan T. Development of a 5 MW reference gearbox for offshore wind turbines. Wind Energy 2015;19(6). http://dx.doi.org/10.1002/we.1884, http://onlinelibrary.wiley.com/doi/10.1002/we.1884/abstract.

[18] Nejad AR, Bachynski EE, Gao Z, Moan T. Fatigue damage comparison of mechanical components in a land-based and a spar floating wind turbine. Procedia Eng 2015;101:330–8. http://dx.doi.org/10.1016/j.proeng.2015.02.040.

[19] Nejad AR, Bachynski EE, Kvittem MI, Luan C, Gao Z, Moan T. Stochastic dynamic load effect and fatigue damage analysis of drivetrains in land-based and TLP, spar and semi-submersible floating wind turbines. Mar Struct 2015;42:137–53. http://dx.doi.org/10.1016/j.marstruc.2015.03.006.

[20] Guo Y, Keller J, LaCava W. Planetary gear load sharing of wind turbine drivetrains subjected to non-torque loads. Wind Energy 2015;18(4):757–68. http://dx.doi.org/10.1002/we.1731.

[21] Guo Y, Bergua RvDJ, Jove J, Campbell J. Improved wind turbine drivetrain designs to minimize the impacts of non-torque loads. Wind Energy 2015;18(12). http://dx.doi.org/10.1002/we.1815, http://onlinelibrary.wiley.com/store/10.1002/we.1815/asset/we1815.pdf?v=1{&}t=j69kdal1&s=14281431866904c3299d35a692bc66419a6f52dc.

[22] Hart E, Clarke B, Nicholas G, Kazemi Amiri A, Stirling J, Carroll J, et al. A review of wind turbine main bearings: Design, operation, modelling, damage mechanisms and fault detection. 2020, p. 105–24. http://dx.doi.org/10.5194/wes-5-105-2020.

[23] Xing Y, Karimirad M, Moan T. Modelling and analysis of floating spar-type wind turbine drivetrain. Wind Energy 2014;17(4):565–87. http://dx.doi.org/10.1002/we.1590.

[24] Jonkman J, Musial W. Offshore code comparison collaboration (OC3) for IEA wind task 23 offshore wind technology and deployment. Technical Report, Golden, CO (United States): National Renewable Energy Lab.(NREL); 2010.

[25] Jonkman J, Butterfield S, Musial W, Scott G, Usdoe. Definition of a 5-MW reference wind turbine for offshore system development. Tecnical Report NREL/TP-500-38060, National Renewable Energy Laboratory (U.S.); 2009, http://dx.doi.org/10.2172/947422, http://www.nrel.gov/docs/fy09osti/38060.pdf.
[26] Goupee AJ, Koo BJ, Kimball RW, Lambrakos KF, Dagher HJ. Experimental comparison of three floating wind turbine concepts. J Offshore Mech Arct Eng 2014;136(2):20906.
[27] IECRE OD-501 - IEC system for certification to standards relating to equipment for use in renewable energy applications (IECRE system) - type and component certification scheme. 2018.
[28] IEC 61400 - wind turbines - part 22: Conformity testing and certification. 2011.
[29] IEC 61400 - wind turbines - part 13: Measurement of mechanical loads. 2015.
[30] IEC 61400 - wind turbines - part 4: Design requirements for wind turbine gearboxes. 2012.
[31] DNVGL-ST-0361 machinery for wind turbines. 2016, http://www.dnvgl.com.
[32] Hoffmann L, Müller MS, Sommavilla M, Koch AW. Wälzlagerüberwachung mit faseroptischer Sensorik. Monit. Roll. Bear. Fiber Opt. Sens. 2007;74(4):204–10. http://dx.doi.org/10.1524/teme.2007.74.4.204.
[33] Oliver X, de Saracibar CA. Continuum mechanics for engineers: theory and problems. 2017, p. 1–13. http://dx.doi.org/10.13140/RG.2.2.25821.20961.
[34] Seidel BS, Erdelyi EA. On the vibration of a thick ring in its own plane. J Eng Ind 1964;86(3):240. http://dx.doi.org/10.1115/1.3670524, http://manufacturingscience.asmedigitalcollection.asme.org/pdfaccess.ashx?url=/data/journals/jmsefk/27484/240_1.pdf.
[35] Soedel W. Vibrations of shells and plates. Mechanical engineering. 3rd ed.. Vol. 177, New York: Marcel Dekker; 2004.
[36] Olver PJ. Introduction to partial differential equations. Undergraduate texts in mathematics, Cham: Springer International Publishing; 2014, http://dx.doi.org/10.1007/978-3-319-02099-0, http://link.springer.com/10.1007/978-3-319-02099-0.